NEW INSIGHTS INTO THE PROPERTIES DETERMINING OXYGEN VACANCY FORMATION ENERGIES IN OXIDES

by

Ann M. Deml

A thesis submitted to the Faculty and the Board of Trustees of the Colorado School of Mines in partial fulfillment of the requirements for the degree of Doctor of Philosophy (Materials Science).

Golden, Colorado

Date _____

Signed: _____
Ann Deml

Signed: _____
Ryan O'Hayre
Thesis Advisor

Signed: _____
Charles B. Musgrave
Thesis Advisor

Golden, Colorado

Date _____

Signed: _____
Dr. Brian Gorman
Materials Science Program Director

ABSTRACT

Oxygen vacancy formation energies play a fundamental role in a broad range of important energy applications; nevertheless, predictive understanding of the properties of metal oxides that determine such energetics remains incomplete. We use modern, electronic structure theory and solid state defect models to demonstrate a fundamental and unifying set of intrinsic bulk material properties which serve as accurate descriptors of oxygen vacancy formation energies across a wide variety of oxides spanning a range of different crystal structures. This thesis work shows oxygen vacancy formation energies increase with increasing metal-oxygen bond strength and/or increasing oxygen vacancy electron redistribution energy. Here, the bond strength contribution is closely related to the oxide enthalpy of formation and the electron redistribution energy contribution is described by either the band gap energy or, for small band gap materials, by the energy difference between the lowest unoccupied state and the O *2p* band center. Our findings i) provide a valuable method for efficiently predicting oxygen vacancy formation energies from intrinsic bulk material properties and ii) extend our understanding of the dominant physical mechanisms contributing to oxygen vacancy formation energies thereby better enabling the design of new redox active materials.

TABLE OF CONTENTS

LIST OF FIGURES

LIST OF TABLES

ACKNOWLEDGEMENTS

It is a great pleasure to acknowledge those who have contributed both to my research experience and my personal growth over the last years. I am particularly grateful for the support and guidance of my advisors, Profs. Ryan O'Hayre, Vladan Stevanović, and Charles Musgrave. Each has played a direct role in mentoring my development as a researcher, and I have been continually grateful to have three different people so highly invested in my success. I am also appreciative of my thesis committee members, Profs. Mark Lusk, Jianhua Tong, and Will Medlin. They have kindly contributed to the development of a quality thesis.

I also wish to acknowledge my group members both at the Colorado School of Mines and the University of Colorado Boulder for our frequent discussions and interactions. I gratefully acknowledge financial support from the Renewable Energy Materials Research Science and Engineering Center, the Department of Energy Office of Science Research Fellowship, and the National Science Foundation.

Finally, I wish to express my sincerest gratitude to my family and friends. It is these people that have most significantly influenced my experience and made it an important segment in this great adventure of life.

CHAPTER 1

INTRODUCTION

A broad range of important energy applications such as solar thermochemical fuel production cycles, thermochemical heat storage cycles, solid oxide fuel cells, oxygen separation membranes, and catalytic membrane reactors utilize metal oxide components whose performance depends critically on the participation of oxygen vacancies V_O. The removal (or uptake) of oxygen ions from these metal oxides involves the formation (or filling) of V_O, and while modern theoretical tools can accurately compute oxygen vacancy formation energies E_V on a case-by-case basis,[1] predictive understanding of V_O formation energetics across broader classes of metal oxide materials is just developing.[2–5] As discussed in detail throughout the following chapters, a few previous studies have examined the material dependence of E_V within relatively small groups of similar oxides; however, we have developed a fundamental and unifying set of E_V descriptors that applies across broad variations in oxide composition including different crystal structures.

The formation of an oxygen vacancy involves the removal of a neutral oxygen atom thereby requiring energy to i) break metal-oxygen bonds and ii) redistribute the electrons that had previously participated in bonds with the removed oxygen atom. In this work, we connect these basic mechanisms of V_O formation with the material properties that dictate E_V. To do so, we use first principles quantum mechanical methods as a powerful tool to investigate the fundamental phenomena associated with V_O formation and their composition dependence. Calculations of E_V, electronic structure, and charge distributions in stoichiometric and oxygen deficient structures provide insights into V_O formation energetics, the corresponding electron density redistribution, and variations due to composition.

In particular, calculated densities of states (DOS) serve as a value tool for investigations of the composition dependence of electronic structure. For example, DOS can be used to analyze the redistribution of O *2p* electrons associated with V_O formation as shown schematically in Figure 1.1 for oxides with zero, small, and large band gaps. Transition metal

(TM) oxides commonly exhibit a TM *3d* band which lies above the O *2p* band with regard to energy. In the case of a zero band gap oxide, the boundary between the low energy occupied states and the higher energy unoccupied states is given by the Fermi energy E_F which is equivalent to the energy of the lowest unoccupied state E_{LUS}. The E_F can be shifted by tuning the oxide composition as will be discussed further in later chapters. For such zero band gap oxides, V_O formation results in redistribution of O *2p* electrons to E_F as shown in Figure 1.1. In contrast, finite band gap oxides exhibit an energy range over which there are no available electronic states. As a result, V_O formation in finite band gap oxides results in redistribution of O *2p* electrons either to the lowest energy unoccupied states at the conduction band edge or to V_O-induced defect states within the band gap, as shown in Figure 1.1. These composition dependences of the electronic structures of oxides provide useful insights into the mechanisms of V_O formation and will be referenced throughout the following chapters.

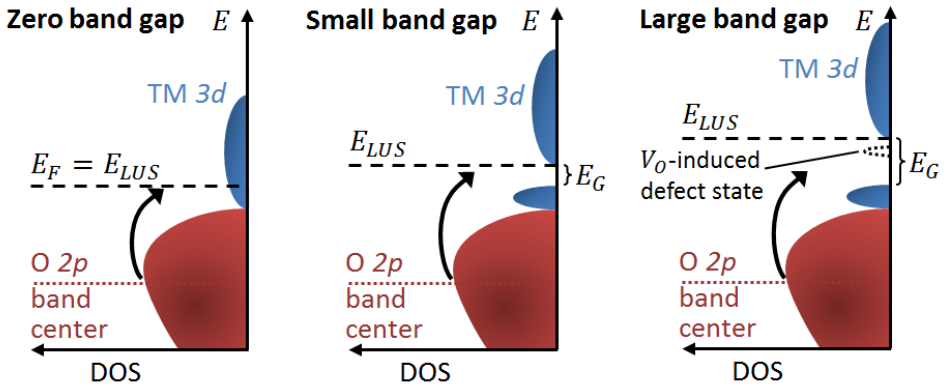

Figure 1.1 Schematic densities of states (DOS) for oxides with zero, small, and large band gaps show differences in the redistribution of O *2p* electrons associated with V_O formation. The transition metal (TM) *3d* and O *2p* bands are shown in blue and red, respectively, and the Fermi energy E_F or the energy of lowest unoccupied state E_{LUS} is denoted by the dashed line.

Much of this work focuses on perovskite oxides due to the structural versatility of the crystal structure. A generic ABO_3 perovskite composition commonly consists of a large 3+ cation on the A-site with a smaller 3+ cation that is octahedrally coordinated to its neighboring O ions on the B-site, as shown in Figure 1.2. This structure exhibits a high tolerance for extensive cation substitution on either or both the A and B-sites. Substitutional cations may exhibit the same or different oxidation states resulting in significant tunability of the material composition and properties. Perovskite oxides also exhibit high tolerance for large O nonstoichiometries,

good catalytic properties, and good structural stability. In this thesis, we present our investigation of V_O formation energies via a series of perovskite materials systems of increasingly broad composition before ultimately expanding our treatment to a range of other crystal structures.

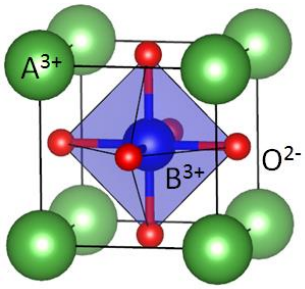

Figure 1.2 A generic ABO_3 perovskite unit cell with a large 3+ cation on the A-site and a smaller 3+ cation that is octahedrally coordinated to its neighboring O ions on the B-site.

To begin, in Chapter 2, we use a combination of *ab initio* and experimental techniques to investigate the composition dependence of oxygen vacancy formation energies E_V in the complex perovskite $Sr_xLa_{1-x}Mn_yAl_{1-y}O_3$ (SLMA), a material system demonstrated to significantly outperform the previous state-of-the-art material, ceria, for solar thermochemical (STC) fuel production. STC redox cycles utilize an active oxide material to facilitate the splitting of H_2O or CO_2. Commonly, a thermal reduction reaction generates oxygen vacancies under high temperatures in the first step, and in the second step, a gas-splitting reaction reoxidizes the nonstoichiometric metal oxide to produce H_2 and/or CO. As a result, the energy to form oxygen vacancies is a critical determinant of material performance for STC cycles. Our density functional theory calculations predict that E_V as a function of composition spans a large range from near 0 to over 3 eV under standard conditions and exhibits trends consistent with our equilibrium oxygen nonstoichiometries determined using thermogravimetric analysis. Our findings show that the strong sensitivity of E_V to composition arises from the composition dependence of the Fermi energy relative to the O *2p* band center. From these results, we identify the range of E_V particularly suited for STC cycles for a given set of reduction and oxidation reaction conditions and present a materials design strategy for optimization of E_V through compositional tuning.

In Chapter 3, we present a study of V_O formation in $La_{1-x}Sr_xBO_3$ perovskites (B=Cr, Mn, Fe, Co, and Ni). Compared to SLMA, this family of perovskites shows an even wider range of E_V spanning from near 0 to over 5 eV and includes compositions which are metallic as well as compositions that are wide band gap insulators. For this broader family of perovskites, we demonstrate that a combination of two fundamental and intrinsic materials properties, the oxide enthalpy of formation $\Delta H_{f,oxide}$ and the minimum band gap energy, accurately correlate with E_V. The energy to form a single, neutral oxygen vacancy decreases with both $\Delta H_{f,oxide}$ and the band gap energy in agreement with the relation of the former to metal-oxygen bond strengths and of the latter to the energy of the oxygen vacancy electron redistribution. These findings extend our understanding of the nature of V_O formation in oxides with a band gap.

Finally, in Chapter 4, we investigate the unifying fundamental phenomena associated with V_O formation and its material dependence across a broad range of compositions and crystal structures. We first examine intrinsic bulk material properties which describe E_V in perovskite oxides and find that, for small band gap perovskites, a combination of $\Delta H_{f,oxide}$ and the energy of the lowest unoccupied state relative to the O *2p* band center accurately correlate with E_V. For larger band gap oxides, a combination of the $\Delta H_{f,oxide}$ and the band gap energy correlate with E_V. In both cases, the first term relates to the metal-oxygen bond strengths and the second relates to the energetic redistribution of the oxygen vacancy electrons. We use both DFT+U and more accurate GW band gap energies to confirm the accuracy of these descriptors. Finally, we demonstrate $\Delta H_{f,oxide}$ and the band gap energy to be accurate descriptors of E_V for a broad range of oxides with GW band gap energies greater than 1 eV including those with perovskite, antifluorite, corundum, rock salt, and rutile crystal structures.

Surprisingly, the physical mechanisms that contribute most significantly to E_V are quite simple and broadly applicable. Namely, E_V increases with increasing metal-oxygen bond strength and/or increasing V_O electron redistribution energy, as indicated by more negative $\Delta H_{f,oxide}$ and larger band gap energies (or, for small band gap materials, larger energy differences between the lowest unoccupied state and the O *2p* band center), respectively. These findings extend our understanding of the dominant physical mechanisms contributing to E_V in oxides and provide a valuable method for efficiently predicting E_V from intrinsic bulk

material properties. We suggest the application of this work for the informed design and study of novel oxide systems for a range of technological applications.

1.1 References

1. H. Peng, D. O. Scanlon, V. Stevanović, J. Vidal, G. W. Watson, and S. Lany, *Phys. Rev. B*, 2013, **88**, 115201.
2. A. M. Deml, V. Stevanović, C. L. Muhich, C. B. Musgrave, and R. O'Hayre, *Energy Environ. Sci*., 2014, **7**, 1996–2004.
3. A. M. Deml, V. Stevanović, A. M. Holder, M. Sanders, C. B. Musgrave, and R. O'Hayre, *Nat. Commun*. (submitted).
4. R. Merkle, Y. A. Mastrikov, E. A. Kotomin, M. M. Kuklja, and J. Maier, *J. Electrochem. Soc*., 2012, **159**, B219–B226.
5. Y. A. Mastrikov, R. Merkle, E. A. Kotomin, M. M. Kuklja, and J. Maier, *Phys. Chem. Chem. Phys.*, 2013, **15**, 911–918.

CHAPTER 2

TUNABLE OXYGEN VACANCY FORMATION ENERGETICS IN THE COMPLEX PEROVSKITE OXIDE $Sr_xLa_{1-x}Mn_yAl_{1-y}O_3$

A paper submitted to *Nature Communications*

Ann M. Deml,[1,2,†] Vladan Stevanović,[3,4] Aaron M. Holder,[2,5] Michael Sanders,[1] Ryan O'Hayre,[1,*] and Charles B. Musgrave,[2,5,*]

[1] Department of Metallurgical and Materials Engineering, Colorado School of Mines, Golden, Colorado 80401, USA
[2] Department of Chemical and Biological Engineering, University of Colorado Boulder, Boulder, Colorado 80303, USA
[3] Department of Physics, Colorado School of Mines, Golden, Colorado 80401, USA
[4] National Renewable Energy Laboratory, Golden, Colorado 80401, USA
[5] Department of Chemistry and Biochemistry, University of Colorado Boulder, Boulder, Colorado 80309, USA
* Corresponding authors
[†] A.M.D. performed the DFT calculations and analysis with the support of V.S. and A.M.H. M.S. carried out the TGA experiments and analysis. A.M.D. wrote the manuscript. All authors discussed the data and edited the manuscript.

2.1 Abstract

The composition dependence of oxygen vacancy formation energies E_V in the complex perovskite $Sr_xLa_{1-x}Mn_yAl_{1-y}O_3$, a material system demonstrated to significantly outperform ceria for solar thermochemical (STC) fuel production, was investigated using a combination of *ab initio* and experimental techniques. Density functional theory calculations predict that E_V as a function of composition spans a large range from near 0 to over 3 eV under standard conditions and exhibits trends consistent with our equilibrium oxygen nonstoichiometries determined using thermogravimetric analysis. Our findings show that the strong sensitivity of E_V to composition arises from the composition dependence of the Fermi energy relative to the O *2p* band center. From these results, we identify the range of E_V particularly suited for STC cycles for a given set of reduction and oxidation reaction conditions and present a materials design strategy for optimization of E_V through compositional tuning.

2.2 Introduction

Solar thermochemical (STC) fuel production cycles have recently attracted significant attention for their potential to efficiently produce renewable chemical fuels.[1–4] These two-step redox cycles utilize an active oxide material to facilitate the splitting of water or carbon dioxide. Commonly, a thermal reduction reaction generates oxygen vacancies under high temperatures in the first step, and in the second step, a gas-splitting reaction reoxidizes the nonstoichiometric metal oxide to produce H_2 and/or CO. Alternatively, the redox cycle can occur between distinct oxidized and reduced phases; however, our focus here is on nonstoichiometric systems because of their superior kinetics and selectivity.[2] At STC temperatures where thermodynamics dominate over kinetics, the performance of a given nonstoichiometric oxide for STC H_2 and/or CO production is largely determined by the enthalpy of the thermal reduction reaction and the redox capacity (maximum reversible oxygen nonstoichiometry) of the oxide.[5,6] Furthermore, because the enthalpy of the thermal reduction reaction primarily depends on the energy to form oxygen vacancies, only oxides with oxygen vacancy formation energies E_V within a specific range are viable STC redox materials. In other words, the materials should not be too easily reduced nor too easily reoxidized.

A major challenge to the widespread use of STC fuel cycles is a lack of suitable active materials which can be efficiently cycled for industrial scale processes. A new perovskite system $Sr_xLa_{1-x}Mn_yAl_{1-y}O_3$ (SLMA) was recently shown to exhibit fast kinetics and 9x higher H_2 yields in STC water-splitting than the previous state-of-the-art material, ceria, when reduced at 1623 K in He and reoxidized at 1273 K in 40 vol% H_2O.[4] Three specific SLMA compositions were reported, in order of increasing hydrogen production: $Sr_{0.4}La_{0.6}Mn_{0.4}Al_{0.6}O_3$ < $Sr_{0.6}La_{0.4}Mn_{0.6}Al_{0.4}O_3$ < $Sr_{0.4}La_{0.6}Mn_{0.6}Al_{0.4}O_3$. These compositions showed good structural stability, began to evolve O_2 at temperatures as much as 300 °C below ceria, and also exhibited 6x greater CO yields than ceria under similar conditions. Related perovskite systems $La_xA_{1-x}Fe_yB_{1-y}O_3$ (A=Sr, Ce and B=Co, Mn) have also recently been reported to exhibit improved CO production over ceria.[7] Although STC cycles utilizing ceria are feasible, ceria requires high reduction temperatures (>1773 K) to achieve even small oxygen deficiencies (oxygen nonstoichiometry << 0.1) which in turn limits these systems to low redox capacities and low efficiencies.[2,3,7] It has been proposed that the

greater compositional flexibility of perovskite systems compared to ceria enables better optimization of E_V,[4] resulting in significantly better STC performance than ceria.

In this work, we focus on and investigate the composition dependence of E_V for positively charged oxygen vacancies across the SLMA composition spectrum using a combination of computation and experiment in order to reveal the origins of the superior STC performance of SLMA over ceria. Additionally, our results i) allow for identification of the material independent range of E_V that is particularly suitable for STC applications depending on the reduction and oxidation reaction conditions and ii) provide a materials design strategy for the optimization of E_V through compositional tuning. Our insights into the origins of the SLMA composition dependence of E_V are also broadly applicable for the informed design of other complex oxides for a range of important energy applications including solar thermochemical heat storage, solid oxide fuel cells, oxygen separation membranes, and catalytic membrane reactors.

Although V_O formation has been extensively studied in numerous simple oxide compositions,[8–12] computational studies of multicomponent oxides across a range of compositions have been limited. Notable exceptions include studies of $Ba_{1-x}Sr_xCo_{1-y}Fe_yO_3$ and $La_{1-x}Sr_xCo_{1-y}Fe_yO_3$ which show that E_V increases linearly with Fe content.[13–15] The $La_{1-x}Sr_xCo_{1-y}Fe_yO_3$[15] and $La_{1-x}Sr_xMnO_3$[16] systems have also been shown to exhibit increasing E_V with increasing Sr content due to the resultant increases in hole density. Nevertheless, only a limited number of compositions have been studied for each system. Another related study of $La_{1-x}Sr_xCo_{1-y}Fe_yO_3$ focused on the temperature dependence of E_V[17] but also only considered select compositions. Similarly, a study of V_O formation in $La_{1-x}Sr_xGa_{1-y}Mg_yO_3$ investigated only one particular composition.[18] Experimental studies of $La_{1-x}Sr_xCo_{1-y}Fe_yO_3$ show less negative enthalpies of oxidation (larger E_V) with increasing Fe content[19] while studies of $La_{1-x}Sr_xCrO_3$, $La_{1-x}Sr_xFeO_3$, and $La_{1-x}Ca_xCrO_3$ systems show less negative enthalpies of oxidation with increasing Sr and Ca content, respectively.[20,21] Again, however, only a limited number of compositions and/or changes in only one component of the composition were examined for each system.

Herein, we use first principles electronic structure calculations to predict oxygen vacancy formation energies E_V spanning a range from near 0 to over 3 eV for 16 different SLMA

compositions, assuming standard temperature and oxygen partial pressure conditions. Our results demonstrate that the strong composition dependence of E_V is mainly due to the composition dependence of the Fermi energy E_F relative to the center of the O *2p* electronic band. This is because the formation of an oxygen vacancy requires both the spatial and energetic redistribution of O *2p* electron density that had previously participated in bonds with the removed oxygen atom. This electron density redistributes to occupy the lowest energy unoccupied states present upon forming the oxygen vacancy which, for SLMA, are located within the valence band at E_F due to the aliovalent substitution of Sr^{2+} onto La^{3+} sites. Additionally, the inclusion of Mn introduces a mixed character Mn *3d*-O *2p* band that lies higher in energy than the O *2p* band and creates a large range over which E_F can be shifted. Therefore, it is the relative mole fraction of Sr and Mn ($\chi_{Sr} - \chi_{Mn}$) that dictates the character and energy of the states at E_F and consequently the magnitude of E_V. This E_V dependence on the energy difference between E_F and the O *2p* band center is analogous to the Fermi level dependence of charged defect formation energies in standard insulating and semiconducting systems.[9,22,23] Our results ultimately demonstrate that the experimental observation[4] of superior STC performance of SLMA over ceria is due to both better redox thermodynamics and the resultant increased redox capacity.

Motivated by our computational findings, we experimentally examine the composition dependence of the oxygen nonstoichiometry of six different SLMA compositions under reducing conditions. All samples were synthesized using a solid state reaction synthesis method and characterized using thermogravimetric analysis (TGA) to measure changes in oxygen nonstoichiometry for samples equilibrated under oxidizing conditions (room temperature in air) compared to reducing conditions (1273 K, P_{O_2} ~10^{-5} atm). From the combined analysis of computational and experimental data, we find that i) the primary contribution to measured changes in oxygen nonstoichiometry is given by the E_V of a single oxygen vacancy and ii) under operating conditions similar to those reported by McDaniel *et al.,*[4] the material independent, optimal E_V for STC cycles fall in the range of ~1.9-2.5 eV (values expressed at standard conditions). These bounds ensure thermodynamically favorable V_O formation during the reduction reaction and V_O filling during the reoxidation reaction, under their respective

conditions. Moreover, given that the redox conditions, which may be constrained by kinetic or reactor limitations, define the optimal range of E_V, our results provide a route for designing complex oxides for STC cycles. Specifically, aliovalent A-site substitution in perovskites can be used to shift E_F to lower energies thereby decreasing E_V; likewise, inclusion of early to mid *3d* transition metals on the B-site can provide a larger range over which to tune E_V by adjusting the relative A and B-site compositions.

2.3 Results

Herein, we provide the results of our combined computational and experimental investigation of the vacancy formation energetics of SLMA.

2.3.1 Oxygen vacancy formation energies

We calculate the formation energy of the charged 2+ state of an oxygen vacancy (hereafter simply referred to as an oxygen vacancy) at standard conditions for 16 different SLMA compositions using the standard supercell approach based on DFT+U[9] according to

$$E_V = E_{tot}^{defect} - E_{tot}^{host} + \mu_O^{FERE}$$

where E_o^{defect} and E_o^{host} are the total energies of the oxygen deficient (defect) and stoichiometric (host) supercells, respectively, and μ_O^{FERE} is the standard state oxygen chemical potential derived from the fitted elemental-phase reference energies (FERE)[24] approach. Although this equation generally refers to the case of neutral oxygen vacancies, the vacancies in our calculations are effectively in the charged 2+ state because SLMA compositions primarily exhibit metallic character with E_F inside the valence band in which case, unlike for semiconductors and insulators, charges freely exchange with the reservoir characterized by E_F to occupy valence band states. We check the configuration dependence of E_V by performing calculations for two different random cation configurations for each composition each with four different randomly chosen oxygen vacancy sites. In Figure 2.1(a) and throughout the document, we report average E_V values for the set of different cation and oxygen vacancy configurations with error bars corresponding to the standard deviation of E_V. Additional information is provided in the Computational Details.

The SLMA composition spectrum exhibits a large range of E_V, spanning from near 0 to more than 3 eV as shown in Figure 2.1(a), thereby enabling highly tunable V_O formation

energetics and consequently redox properties. We find that E_V decreases with increasing mole fractions of Sr χ_{Sr} and either increases or remains nearly constant with increasing mole fractions of Mn χ_{Mn}. As a result, E_V is higher for compositions with small χ_{Sr} and lower for compositions that combine large χ_{Sr} and small χ_{Mn}.

Trends in our predicted composition dependence of E_V are strongly corroborated by experimental measurements of the changes in oxygen nonstoichiometry for samples in thermodynamic equilibrium under oxidizing conditions (room temperature in air) compared to reducing conditions (1273 K, P_{O_2} ~10^{-5} atm) as shown in Figure 2.1(b). Here, specific $Sr_xLa_{1-x}Mn_yAl_{1-y}O_3$ compositions are denoted as SLMA$\alpha\beta\gamma\varepsilon$, e.g. SLMA2864 denotes a composition of $Sr_{0.2}La_{0.8}Mn_{0.6}Al_{0.4}O_3$. The measured exponential decrease in oxygen nonstoichiometry with increasing predicted E_V indicates that the dominant thermodynamic contribution to V_O formation under these conditions is indeed the energy to form a single oxygen vacancy.

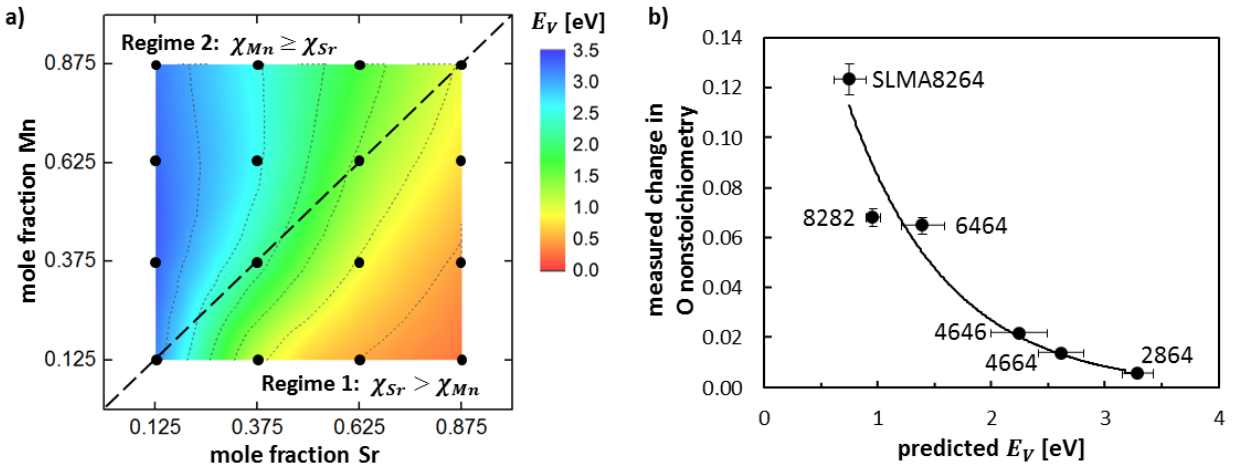

Figure 2.1 Oxygen vacancy formation energies. a) DFT+U calculated oxygen vacancy formation energies E_V for the SLMA composition spectrum show that E_V decreases with increasing mole fractions of Sr χ_{Sr} and either increases or remains nearly constant with increasing mole fractions of Mn χ_{Mn}. The composition dependence of E_V exhibits two regimes differentiated by the relative χ_{Sr} and χ_{Mn}. Calculated compositions are marked by black points; a linear interpolation scheme was used to generate contour lines and the color scheme. b) Trends in the predicted E_V are supported by good agreement via an exponential fit with measured changes in oxygen nonstoichiometries under reducing conditions (1273 K, P_{O_2} ~10^{-5} atm). Labels specify the specific SLMA compositions (see text for details).

All compositions shown in Figure 2.1(a) exhibit decreasing E_V with increasing χ_{Sr}. Further analysis of the composition dependence reveals two mechanistic regimes for V_O

formation (Figure 2.2). First, the rate of decrease in E_V with increasing χ_{Sr} is smaller for compositions in Regime 1 where $\chi_{Sr} > \chi_{Mn}$ than for those in Regime 2 where $\chi_{Mn} \geq \chi_{Sr}$, as indicated by the difference in slopes between the dotted and dashed lines, respectively. Second, increases in χ_{Mn} within Regime 1 result in increasing E_V as shown by the vertical offset of the two dotted lines. In contrast, increases in χ_{Mn} within Regime 2 result in approximately constant E_V as shown by the single dashed line. Figure 2.2 also shows that the linear decrease in E_V with increasing χ_{Sr} for Regime 2 extends to endmembers such as $LaMnO_3$ (LM) and $La_{0.6}Sr_{0.4}MnO_3$ (LSM64) for which experimental data is available. Our calculated values of E_V for LM and LSM64 (3.9±0.1 and 2.6±0.1 eV, respectively) are consistent with experimental thermogravimetric measurements of the reaction enthalpies for oxidation by $O_{2(g)}$ (-3.7±0.1 and -2.9±0.1 eV, respectively; see Supplementary Information)[25,26] providing additional validation of our method for calculating E_V. The behavior of Regime 2 is also consistent with E_V calculations for $La_{1-x}Sr_xCo_{1-y}Fe_yO_3$ (where $\chi_{Co} + \chi_{Fe} \geq \chi_{Sr}$) which show that E_V decreases with increasing Sr content.[15]

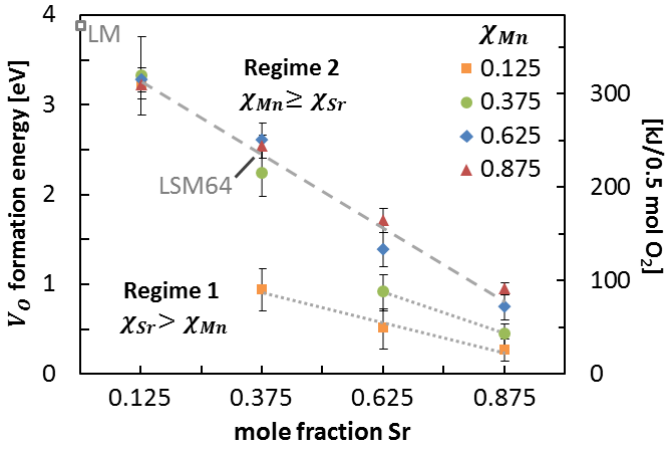

Figure 2.2 Composition regimes for oxygen vacancy formation. The calculated trends in oxygen vacancy formation energies E_V from Figure 2.1(a) exhibit two composition regimes based on the relative mole fractions of Sr and Mn (χ_{Sr} and χ_{Mn}). Compositions in Regime 1 where $\chi_{Sr} > \chi_{Mn}$ exhibit smaller decreases in E_V with increasing χ_{Sr} and larger increases in E_V with increasing χ_{Mn} than those in Regime 2 where $\chi_{Mn} \geq \chi_{Sr}$. The dotted and dashed lines indicate trends in E_V within Regimes 1 and 2, respectively.

The trend of decreasing predicted E_V with increasing χ_{Sr} is corroborated by our experimental results reported in Figure 2.1(b) which show that oxygen nonstoichiometry increases with increasing χ_{Sr} in SLMA2864, SLMA4664, SLMA6464, and SLMA8264.

Additionally, all measured compositions follow the same exponential fit indicating that changes in the measured oxygen nonstoichiometry upon reduction are approximately equal to the absolute oxygen nonstoichiometries of the reduced samples. As a result, all compositions are estimated to exhibit negligible oxygen nonstoichiometry at room temperature in air which is consistent with our predictions of thermodynamically unfavorable (positive) reduction reaction energies under such conditions. (From the ideal gas equation of state, the oxygen chemical potential at room temperature in air decreases the reduction reaction energy by ~0.3 eV compared to the predicted E_V under standard conditions. Because the predicted E_V are greater than ~0.3 eV for all measured compositions, the reduction reaction energy is positive and unfavorable under these oxidizing conditions. A detailed discussion of the temperature and oxygen partial pressure dependences of E_V is provided below.)

2.3.2 Electronic structure origins of E_V composition dependence

Our results and the analysis that follows show that the dominant contribution to the composition dependence of E_V within the SLMA composition spectrum arises from the composition dependence of the Fermi energy E_F relative to the O *2p* band center, as shown in Figure 2.3(a). This dependence can be understood from the general mechanism of V_O formation. The formation of an oxygen vacancy requires spatial and energetic redistribution of the O *2p* electrons that previously participated in bonding with the removed oxygen. On V_O formation this electron density is redistributed to occupy the lowest energy unoccupied states which, for oxides without a band gap (e.g. most of the SLMA compositions), are located at E_F. For insulators, however, these electrons populate V_O-induced defect states which often lie within the band gap. Two SLMA compositions, $Sr_{0.2}La_{0.8}Mn_{0.2}Al_{0.8}O_3$ and $Sr_{0.4}La_{0.6}Mn_{0.4}Al_{0.6}O_3$, exhibit finite band gaps. For these compositions the bounds on the energy difference between the V_O-induced defect states and the O *2p* band center are given by the energies of the valence band maximum and the conduction band minimum relative to the O *2p* band center, as shown in Figure 2.3(a) by the open squares and circles, respectively. From these two compositions, it is evident that the energy difference dictating E_V falls within these bounds but requires additional information about the energy of the defect states. Our results are consistent with previous observations correlating the O *2p* band center to the E_V of simple perovskites with zero band

gaps[27] ($LaBO_3$, B=Mn, Co, Ni) and with the catalytic activity of oxygen reduction[27] and evolution reactions[28] suggesting that the dominant mechanisms in these reactions are closely related to bulk V_O formation.

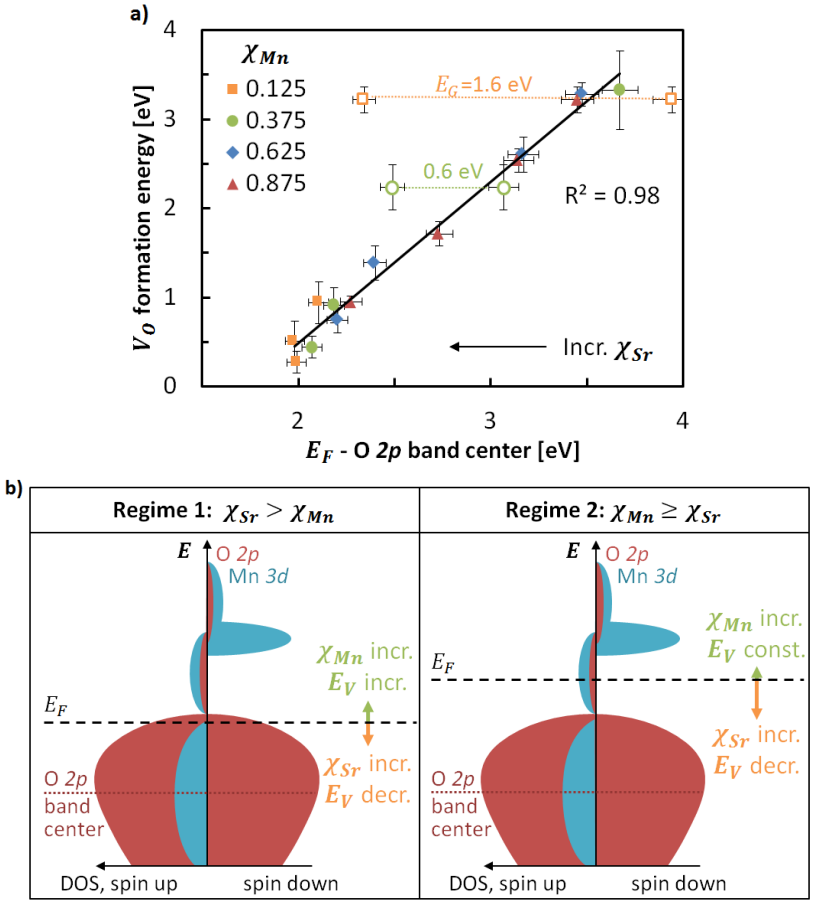

Figure 2.3 Electronic structure mechanisms of V_O formation. a) Computed oxygen vacancy formation energies E_V demonstrate that the energy difference between the Fermi energy E_F and the O *2p* band center provides the dominant contribution to E_V. Open symbols, which are not included in the fit, indicate the bounds on the energy difference between the oxygen vacancy induced defect states and the O *2p* band center for compositions with finite band gaps E_G. b) A schematic of the Mn and O partial densities of states (PDOS) illustrates the connections between the SLMA composition dependence of E_V and the corresponding electronic structure changes. Characteristic properties of the PDOS within Regimes 1 and 2 are shown (left and right, respectively). Changes in E_F and E_V resulting from increasing Sr and Mn mole fractions are denoted in orange and green, respectively, with arrow lengths indicating relative differences in the magnitudes of the E_F shifts. Spin-up and spin-down PDOS are shown left and right of the energy axes, respectively.

The electronic structure origins and composition dependence of E_F relative to the O *2p* band center, and therefore E_V, are summarized schematically in Figure 2.3(b). As discussed in

detail below, the two panels illustrate characteristic properties of the Mn *3d* and O *2p* partial densities of states (PDOS) in each regime along with changes in E_F due to either increasing χ_{Sr} or χ_{Mn}. (Sr, La, and Al PDOS are negligible over these energy ranges.) Conceptually, Sr-substitution onto La crystal lattice sites in SLMA results in an effective 2+ cation on a 3+ site, which introduces holes and shifts E_F into the valence band. The resultant low energy, unoccupied (acceptor) states shown in Figure 2.3(b) play a critical role in V_O formation by accepting O *2p* electrons that previously were involved in bonding to the now removed O atom. It is useful to note that both χ_{Sr} and χ_{Mn} affect the electronic structure due to their respective effects on i) the number of holes resulting from Sr^{2+} substitution onto La^{3+} sites and ii) the character of the corresponding unoccupied states. Also shown in Figure 2.3(b), the partial covalent nature of the Mn-O bonds[29–31] is evidenced by the overlap of the Mn *3d* and O *2p* PDOS. The half-metallic character is consistent with previous DFT+U calculations of $La_{0.7}Sr_{0.3}MnO_3$.[32,33] The corresponding calculated total and partial densities of states of the SLMA composition spectrum are provided in the Supplementary Information, Figure A.1.

2.3.2.1 Differences between Regimes 1 and 2

From Figure 2.3(b), we first examine differences between the electronic structures of compositions in Regimes 1 and 2. For compositions within Regime 1, where $\chi_{Sr} > \chi_{Mn}$, the number of holes from Sr-substitution is greater than the number of states in the mixed character Mn *3d*-O *2p* band (hereafter, Mn-O states). As a result, E_F is located within the O *2p* band and the energy required for redistribution of the electrons is relatively small (E_F is close to the O *2p* band center), which results in lower predicted E_V in Regime 1 compared to Regime 2. On the other hand, for compositions within Regime 2, where $\chi_{Mn} \geq \chi_{Sr}$, the number of holes is less than the number of states in the Mn-O band, and E_F lies within the higher energy Mn-O band. The resultant additional energy required for redistribution of the V_O electrons leads to higher predicted E_V in Regime 2.

Bader charge analysis provides further support for the described composition dependence of the electronic structure of SLMA (Figure A.2). Within Regime 1, the average Bader charge per Mn ion is most positive and predicted to be approximately constant, indicating that Mn ions reach an effective saturation limit beyond which less electron density

(i.e. greater hole density) per Mn ion is unfavorable. This arises due to the high χ_{Sr} and corresponding high hole concentration from Sr-substitution that cannot be fully accommodated by the smaller χ_{Mn}. This behavior is consistent with the fully unoccupied Mn-O band in Regime 1 as shown in Figure 2.3(b). Within Regime 2, the average charge per Mn ion is below its saturation limit indicating that the high χ_{Mn} can accommodate the holes from the smaller χ_{Sr}, which is consistent with the partially occupied Mn-O states of Regime 2 shown in Figure 2.3(b). Variations in the average charge per O ion are more complex and are discussed in detail in the Supplementary Information.

2.3.2.2 Increasing χ_{Sr} with constant χ_{Mn}

We now consider changes in electronic structure resulting from increasing χ_{Sr} with constant χ_{Mn}. Examples of such composition changes in Regimes 1 and 2 are denoted by the orange annotations in Figure 2.3(b). Increasing χ_{Sr} increases the hole concentration due to Sr-substitution on La sites, which produces more unoccupied O *2p* and/or Mn-O states. As a result, E_F shifts to lower energies closer to the O *2p* band center as indicated by the orange arrows in Figure 2.3(b). This decrease in E_F relative to the O *2p* band center results in the predicted decreasing E_V with increasing χ_{Sr}. The E_F shift and the resultant decrease in E_V are smaller for compositions in Regime 1 ($\chi_{Sr} > \chi_{Mn}$) than for those in Regime 2 ($\chi_{Mn} \geq \chi_{Sr}$) due to the higher density of states at E_F in Regime 1 which provides the required increase in the number of unoccupied states over a smaller energy range. Overall, decreases in the energy difference between E_F and the O *2p* band center due to changes in composition decrease E_V by reducing the energetic cost of redistributing the charge density produced by V_O formation. These same V_O formation effects are evidenced by changes in the electronic charge distributions on Mn and O ions (Figure A.2 and associated discussion).

2.3.2.3 Increasing χ_{Mn} with constant χ_{Sr}

We now examine changes in electronic structure that result from increasing χ_{Mn} with constant χ_{Sr}. Examples of such composition changes in Regimes 1 and 2 are denoted by the green annotations in Figure 2.3(b). In these cases, holding χ_{Sr} constant leads to a constant hole concentration and, therefore, a constant sum of unoccupied O *2p* and Mn-O states. The

increasing χ_{Mn} does, however, increase the magnitude of the Mn PDOS, the implications of which we discuss below.

Within Regime 1 ($\chi_{Sr} > \chi_{Mn}$), as χ_{Mn} increases the number of unoccupied Mn-O states also increases. Therefore, to maintain a constant number of holes, the number of unoccupied O *2p* states decreases and E_F shifts to higher energies further from the O *2p* band center. This increase in E_F relative to the O *2p* band center results in the predicted increase of E_V with increasing χ_{Mn} in Regime 1. On the other hand, within Regime 2 ($\chi_{Mn} \geq \chi_{Sr}$), the negligible density of unoccupied O *2p* states and the constraint of a constant total number of holes results in an approximately constant number of unoccupied Mn-O states. In this case, the E_F shift is small and E_V is approximately constant. The same V_O formation mechanisms are also evidenced by changes in the electronic charge distributions on Mn and O ions (Figure A.2 and associated discussion).

2.3.3 Optimal E_V and materials design strategies

The optimal range of E_V for an STC cycle results from the redox reaction conditions which may be constrained by kinetic and/or reactor limitations. To identify the optimal range, we examine the temperature and oxygen partial pressure dependences of E_V. These reaction condition dependencies of E_V, which are largely independent of oxide composition, can be approximated by addition of the corresponding change in oxygen chemical potential using the ideal gas equation of state (see Computational Details). For the STC operating conditions selected by McDaniel *et al.*,[4] it can be shown that the decrease in the oxygen chemical potential under the given thermal reduction conditions (1623 K, P_{O_2} ~10^{-5} atm) is ~2.5 eV relative to standard conditions. Therefore, a thermodynamically favorable (negative) reduction reaction requires a maximum standard state E_V of ~2.5 eV. Similarly, for a thermodynamically favorable reoxidation reaction, the decrease in the oxygen chemical potential under the given reoxidation conditions (1273 K in 40 vol% H_2O), with the approximation of equal or lesser P_{O_2} than the thermal reduction reaction, requires a minimum standard state E_V ≥1.9 eV.

We compare this material independent range of 1.9<E_V<2.5 eV derived for thermodynamically favorable reduction and reoxidation reactions to the predicted E_V for SLMA4664, SLMA6464, and SLMA4646 compositions reported by McDaniel *et al.* to exhibit

excellent STC performance. The predicted E_V of these SLMA compositions (2.6, 1.4, and 2.2 ± 0.2 eV, respectively) all correspond to thermodynamically favorable reduction reactions. In addition, two of the three compositions are predicted to exhibit thermodynamically favorable reoxidation reactions. The measured hydrogen production of the third composition, SLMA6464, is reported to be lower than that of SLMA4664 (despite the higher theoretical redox capacity of SLMA6464) which is likely due to incomplete reoxidation as a result of the low E_V of SLMA6464. This combination of computation and experiment, therefore, indicates that the material independent optimal range of E_V for STC fuel production cycles under similar operating conditions is ~1.9-2.5 eV. This range of E_V corresponds to an optimum activity toward reduction and reoxidation of the oxide for the two-step cycle and explains the superior performance of SLMA over ceria, which is too difficult to reduce (from experiment E_V=4.7 eV under standard conditions[34]). As a result, optimal SLMA compositions with target E_V properties for STC cycles are predicted to lie generally within the range represented by the blue-green region in Figure 2.1(a).

Our insights into the material properties determining E_V also provide a powerful strategy for the informed design of new oxides with target E_V. Starting from a simple oxide with metal constituents each possessing a single oxidation state, the inclusion of a transition metal (TM) species introduces mixed TM-O states which are higher in energy than the O *2p* band, as shown for SLMA in Figure 2.3(b). These TM-O states provide a larger range over which to shift E_F and, consequently, tune E_V. Additionally, aliovalent substitution of a lower valence metal onto the host lattice (e.g. substitution of Sr^{2+} onto La^{3+} lattice sites) can be used to lower E_F and decrease E_V by creating holes or vice versa, as also shown in Figure 2.3(b). In combination, selection of the relative fractions of different metal species facilitates material design and tuning of E_V. Additionally, our results can be used in conjunction with new methods for rapidly predicting E_V[35] to efficiently search for new oxide materials with improved STC performance.

2.4 Discussion

In addition to the redox thermodynamics, the STC performance of a given active material is also dependent on reaction kinetics, utilized redox capacity (oxygen nonstoichiometry), and material stability. The lower temperature of the gas-splitting

reoxidation reaction compared to the thermal reduction reaction generally results in slower kinetics. This gives preference to compositions possessing higher E_V, and correspondingly lower energies for filling V_O, in order to increase the thermodynamic favorability of the reoxidation reaction. For SLMA, higher Sr and Mn fractions increase the number of holes that can be induced by Sr-substitution thereby enabling a greater maximum range of oxygen nonstoichiometry before populating those states. However, it is essential to realize that structural stability likely determines the maximum practical limit on the extent of the oxygen nonstoichiometry. In addition, it has been suggested that the single oxidation state of Al contributes to the observed stability of SLMA[4] implying a practical upper limit on χ_{Mn} as a stability constraint. From these design parameters (redox thermodynamics, kinetics, utilized redox capacity, and material stability), we identify $Sr_{0.4}La_{0.6}Mn_{0.6}Al_{0.4}O_3$ as an optimal SLMA composition for STC fuel production, which is consistent with its measured performance as the best reported SLMA composition. This composition has a predicted E_V=2.6 eV at the upper limit of the recommended E_V range for favorable reaction thermodynamics and reoxidation kinetics. Furthermore, this composition maintains a large fraction of Al for stability. We propose that this approach and understanding of the mechanisms governing the kinetics, redox capacity, stability, and V_O formation energetics of complex oxides can be applied to a wide range of material systems to efficiently design and optimize new oxide materials for improved STC performance.

We have used a combination of computational and experimental techniques to investigate the composition dependence of and physical mechanisms contributing to V_O formation energies in SLMA. Our results show that the strong composition dependence of E_V is due to the composition dependence of the Fermi energy relative to the O *2p* band center. From these results, we identify the range of E_V particularly suitable for STC cycles depending on the reduction and oxidation reaction conditions and provide a materials design strategy for optimization of E_V through compositional tuning. Our insights into the origins of the SLMA composition dependence of E_V are broadly valuable for the informed design of other complex oxides for a range of important energy applications including STC fuel production cycles, solid oxide fuel cells, oxygen separation membranes, and catalytic membrane reactors.

2.5 Methods

Herein, we provide the details of our computational and experimental procedures.

2.5.1 Computational details

Spin polarized DFT+U[36] calculations were performed using a plane wave basis set, the PBE exchange-correlation functional,[37] and the projector augmented wave (PAW) method[38] as implemented in the Vienna Ab-initio Simulation Package (VASP).[39] A Monkhorst-Pack k-point sampling[40] was applied with a constant density corresponding to a 2x2x3 k-point mesh for a 80 atom unit cell resulting in total energies converged to within 3 meV/atom with respect to the number of k points. We chose an energy cutoff of 340 eV corresponding to a value ~20% greater than the highest cutoff energy suggested by the employed pseudopotentials (282 eV for the soft oxygen pseudopotential). A constant U of 3 eV value was used for La and Mn in accordance with the U values used for the FERE method developed by Stevanović *et al.*[24] For Sr, Al, and O, the Hubbard U parameter was set to zero. Atomic charges were evaluated using the Bader charge analysis method.[41,42] The energy of the O *2p* band center was calculated from the O PDOS as the center of mass of the O *2p* band including, when relevant, states above the Fermi energy E_F but excluding O *2p* states hybridized with Mn *3d* states.

Spin degrees of freedom were treated explicitly. We performed a limited search for the DFT+U ground state spin configurations for all compositions. Mn magnetic moments were assigned at random and initialized with high spin values for both net zero antiferromagnetic (AFM) and ferromagnetic (FM) spin configurations. The total energy differences between different AFM configurations were typically calculated to be on the order of ~0.01–0.02 eV/atom, consistent with previous studies.[24,35] We found the FM spin configurations to be energetically equal or more favorable than the AFM spin configurations for all SLMA compositions. This is consistent with previous DFT+U[32,33] and HSE[16] calculations showing $La_{1-x}Sr_xMnO_3$ to be FM and half-metallic. We observed similar trends in E_V with composition for AFM and FM spin configurations and, therefore, have reported only FM results for SLMA. $LaMnO_3$ (LM), on the other hand, is experimentally observed to exhibit an AFM ground state. Calculated AFM total energies were found to be within 0.01 eV/magnetic ion of the FM total energy; thus we used an AFM spin configuration for calculating LM properties.

All SLMA cells were generated by atom substitution of the $LaMnO_3$ experimental structure recorded in the inorganic crystal structure database (ICSD).[43] Random substitutions of Sr for La on the A-site and Al for Mn on the B-site in 80 atom (16 formula unit) supercells were used to sample the composition spectrum. Due to the 16 formula unit supercell size, SLMA$\alpha\beta\gamma\varepsilon$ α, β, γ, and ε values of 2, 4, 6, and 8 correspond to exact mole fractions of 0.125, 0.375, 0.625, and 0.875, respectively. Both lattice parameters and atomic positions were optimized allowing for lattice distortions. Two random cation configurations were calculated for each composition. Structures with an oxygen vacancy were created by removal of a neutral oxygen atom resulting in an oxygen nonstoichiometry of 0.0625. Again, both lattice parameters and atomic positions were optimized. Random cation substitution lowers the symmetry of the system and creates nonequivalent O sites. For this reason, E_V was sampled over four randomly chosen oxygen sites for each cation configuration. The E_V resulting from this scheme are converged to within 0.05 eV of the E_V for 160 atom supercells (oxygen nonstoichiometry = 0.03) with the same geometry optimization procedure. However, as is the case for $Ba_{1-x}Sr_xCo_{1-y}Fe_yO_3$,[14,44] E_V is expected to increase with increasing oxygen nonstoichiometry such that the chosen oxygen nonstoichiometry serves primarily as a reference state. The E_V error bars represent the standard deviation for the set of different cation and oxygen vacancy site configurations.

The formation energy of the charged 2+ state of a single oxygen vacancy under standard conditions was calculated according to

$$E_V = E_{tot}^{defect} - E_{tot}^{host} + \mu_O^{FERE}$$

where E_o^{defect} and E_o^{host} are the total energies of the oxygen deficient (defect) and stoichiometric (host) supercells, respectively, and μ_O^{FERE} is the standard state oxygen chemical potential derived from the FERE[24] approach. The system was charge neutral in all of our calculations; however, because substitution of Sr^{2+} onto La^{3+} lattice sites shifts E_F inside the valence band, charging of the oxygen vacancy occurs naturally. Image charge and potential-alignment corrections were not used[9] due to the explicit charge neutrality of the supercells. Incomplete error cancelation occurs in DFT total energy differences of chemically dissimilar systems such as metals, semiconductors, insulators, and/or gaseous molecules. Alternatively, to

correct for errors in the relative energies, the FERE energies, which have been fit to improve calculated standard state enthalpies of formation, were used. Therefore, our predicted E_V values correspond closely to V_O formation energies under standard temperature and pressure conditions (298 K, 1 atm). The temperature and/or oxygen partial pressure dependences of E_V, which are largely independent of oxide composition, have been approximated by addition of the corresponding change in oxygen chemical potential using the ideal gas equation of state under the assumption of neglecting vibrational degrees of freedom.[24] The calculated values of E_V do not include solid state configurational entropies or thermal corrections due to heat capacity differences between the stoichiometric and oxygen deficient solid state phases, consistent with standard computational approaches for defects in solids.[9] Because these contributions are similar for stoichiometric and oxygen deficient supercells of the same composition, the solid state configurational entropies and thermal corrections at 298 K mostly cancel such that E_V accurately matches V_O formation energies at 298 K. This is consistent with computational studies of $SrTiO_3$, ZnO, $La_{1-x}Sr_xMnO_3$, and $La_{1-x}Sr_xCo_{1-y}Fe_yO_3$ which indicate that phonon contributions to the free energy of V_O formation are small (<0.1 eV) at 298 K and tend to remain relatively small (<0.3 eV) for low oxygen nonstoichiometries (<12 % V_O) even at high temperatures (>1200 K).[16,17,45]

2.5.2 Experimental details

For comparison to our computational predictions, various SLMA compositions were synthesized using a solid state reaction synthesis method.[46] Phase purity was checked using XRD. Reduction experiments to measure oxygen nonstoichiometry at elevated temperatures were carried out using a Setaram SETSYS Evolution TGA with a suspended 130 µL platinum crucible. Sample powders were loosely added until the crucible was filled with an approximate mass of 75 mg. Experiments were run in a flowing gas environment of UHP helium (with an average P_{O_2}=10^{-5} atm as measured with a zirconia oxygen sensor) with isothermal holds of 45 min every 100 K from 1073 to 1273 K. Buoyancy effects were corrected by curve subtraction using a pure alumina sample of the same approximate volume as the SLMA samples. Total mass losses between samples at room temperature in air and under reducing conditions were converted to changes in oxygen nonstoichiometry under the assumption that all losses were

due to V_O formation. The prereduced samples are estimated to exhibit negligible oxygen nonstoichiometry such that the absolute oxygen nonstoichiometries of the reduced samples are approximately equal to the changes in oxygen nonstoichiometry according to arguments provided in the main text.

2.6 Acknowledgements

This research was supported by the National Science Foundation (NSF) through the Renewable Energy Materials Research Science and Engineering Center (REMRSEC) under Grant No. DMR-0820518. V.S. acknowledges support from the National Science Foundation under Grant No. DMR-1309980. R.O. acknowledges support from the Orton Ceramics Foundation. This work utilized the Janus supercomputer, which is supported by the NSF (award number CNS-0821794) and the University of Colorado Boulder. The Janus supercomputer is a joint effort of the University of Colorado Boulder, the University of Colorado Denver, and the National Center for Atmospheric Research. The authors thank J. Tong for valuable discussions and suggestions. C.B.M. is a Fellow of the Materials Science Program and the Renewable and Sustainable Energy Institute of the University of Colorado Boulder and the National Renewable Energy Laboratory.

2.7 References

1. C. Perkins and A. W. Weimer, *AIChE J.*, 2009, **55**, 286–293.
2. W. C. Chueh, C. Falter, M. Abbott, D. Scipio, P. Furler, S. M. Haile, and A. Steinfeld, *Science*, 2010, **330**, 1797–1801.
3. C. L. Muhich, B. W. Evanko, K. C. Weston, P. Lichty, X. Liang, J. Martinek, C. B. Musgrave, and A. W. Weimer, *Science*, 2013, **341**, 540–542.
4. A. H. McDaniel, E. C. Miller, D. Arifin, A. Ambrosini, E. N. Coker, R. O'Hayre, W. C. Chueh, and J. Tong, *Energy Environ. Sci.*, 2013, **6**, 2424–2428.
5. B. Meredig and C. Wolverton, *Phys. Rev. B*, 2009, **80**, 245119.
6. I. Ermanoski, N. P. Siegel, and E. B. Stechel, *J. Sol. Energy Eng.*, 2013, **135**, 031002.
7. Q. Jiang, J. Tong, G. Zhou, Z. Jiang, Z. Li, and C. Li, *Sol. Energy*, 2014, **103**, 425–437.
8. M. V. Ganduglia-Pirovano, A. Hofmann, and J. Sauer, *Surf. Sci. Rep.*, 2007, **62**, 219–270.
9. S. Lany and A. Zunger, *Phys. Rev. B*, 2008, **78**, 235104.
10. W. L. Huang, Q. Zhu, W. Ge, and H. Li, *Comput. Mater. Sci.*, 2011, **50**, 1800–1805.
11. D. Marrocchelli, S. R. Bishop, H. L. Tuller, and B. Yildiz, *Adv. Funct. Mater.*, 2012, **22**, 1958–1965.

12. T. Yamamoto and T. Mizoguchi, *Ceram. Int.*, 2013, **39**, S287–S292.

13. R. Merkle, Y. A. Mastrikov, E. A. Kotomin, M. M. Kuklja, and J. Maier, *J. Electrochem. Soc.*, 2012, **159**, B219–B226.

14. E. A. Kotomin, Y. A. Mastrikov, M. M. Kuklja, R. Merkle, A. Roytburd, and J. Maier, *Solid State Ionics*, 2011, **188**, 1–5.

15. Y. A. Mastrikov, R. Merkle, E. A. Kotomin, M. M. Kuklja, and J. Maier, *Phys. Chem. Chem. Phys.*, 2013, **15**, 911–918.

16. M. Pavone, A. B. Mun, A. M. Ritzmann, and E. A. Carter, *J. Phys. Chem. C*, 2014.

17. D. Gryaznov, M. W. Finnis, R. A. Evarestov, and J. Maier, *Solid State Ionics*, 2014, **254**, 11–16.

18. J. Zhang, E.-J. Liang, Q. Sun, and Y. Jia, *Chinese Phys. B*, 2012, **21**, 047201.

19. E. Bucher, W. Sitte, G. Caraman, V. Cherepanov, T. Aksenova, and M. Ananyev, *Solid State Ionics*, 2006, **177**, 3109–3115.

20. J. Cheng and A. Navrotsky, *J. Solid State Chem.*, 2005, **178**, 234–244.

21. J. Cheng, A. Navrotsky, X. Zhou, and H. U. Anderson, *Chem. Mater.*, 2005, **17**, 2197–2207.

22. H. Peng, D. O. Scanlon, V. Stevanović, J. Vidal, G. W. Watson, and S. Lany, *Phys. Rev. B*, 2013, **88**, 115201.

23. D. West, Y. Y. Sun, and S. B. Zhang, *Appl. Phys. Lett.*, 2012, **101**, 082105.

24. V. Stevanović, S. Lany, X. Zhang, and A. Zunger, *Phys. Rev. B*, 2012, **85**, 115104.

25. J. H. Kuo, H. U. Anderson, and D. M. Sparlin, *J. Solid State Chem.*, 1989, **83**, 52–60.

26. J. Mizusaki, H. Tagawa, K. Naraya, and T. Sasamoto, *Solid State Ionics*, 1991, **49**, 111–118.

27. Y.-L. Lee, J. Kleis, J. Rossmeisl, Y. Shao-Horn, and D. Morgan, *Energy Environ. Sci.*, 2011, **4**, 3966–3970.

28. A. Grimaud, K. J. May, C. E. Carlton, Y.-L. Lee, M. Risch, W. T. Hong, J. Zhou, and Y. Shao-Horn, *Nat. Commun.*, 2013, **4**, 2439.

29. M. M. Kuklja, E. A. Kotomin, R. Merkle, Y. A. Mastrikov, and J. Maier, *Phys. Chem. Chem. Phys.*, 2013, **15**, 5443–5471.

30. J. He and C. Franchini, *Phys. Rev. B*, 2012, **86**, 235117.

31. J. Suntivich, H. a Gasteiger, N. Yabuuchi, H. Nakanishi, J. B. Goodenough, and Y. Shao-Horn, *Nat. Chem.*, 2011, **3**, 546–550.

32. H. Jalili, J. W. Han, Y. Kuru, Z. Cai, and B. Yildiz, *J. Phys. Chem. Lett.*, 2011, **3**, 801–807.

33. J. Pruneda, V. Ferrari, R. Rurali, P. Littlewood, N. Spaldin, and E. Artacho, *Phys. Rev. Lett.*, 2007, **99**, 226101.

34. M. A. Panhans and R. N. Blumenthal, *Solid State Ionics*, 1993, **60**, 279–298.

35. A. M. Deml, V. Stevanović, C. L. Muhich, C. B. Musgrave, and R. O'Hayre, *Energy Environ. Sci.*, 2014, **7**, 1996–2004.

36. S. L. Dudarev, G. A. Botton, S. Y. Savrasov, C. J. Humphreys, and A. P. Sutton, *Phys. Rev. B*, 1998, **57**, 1505–1509.

37. J. P. Perdew, K. Burke, and M. Ernzerhof, *Phys. Rev. Lett.*, 1996, **77**, 3865–3868.

38. P. Blöchl, *Phys. Rev. B*, 1994, **50**, 17953–17979.

39. G. Kresse and J. Furthmüller, *Comput. Mater. Sci.*, 1996, **6**, 15–50.

40. H. Monkhorst and J. Pack, *Phys. Rev. B*, 1976, **13**, 5188–5192.

41. G. Henkelman, A. Arnaldsson, and H. Jónsson, *Comput. Mater. Sci.*, 2006, **36**, 354–360.

42. R. F. W. Bader, *Atoms in molecules: A quantum theory*, Oxford University Press, Oxford, 1990.

43. A. Belsky, M. Hellenbrandt, V. L. Karen, and P. Luksch, *Acta Crystallogr. Sect. B Struct. Sci.*, 2002, **B58**, 364–369.

44. M. M. Kuklja, Y. A. Mastrikov, B. Jansang, and E. A. Kotomin, *J. Phys. Chem. C*, 2012, **116**, 18605–18611.

45. D. Gryaznov, E. Blokhin, A. Sorokine, E. A. Kotomin, R. A. Evarestov, A. Bussmann-Holder, and J. Maier, *J. Phys. Chem. C*, 2013, **117**, 13776–13784.

46. V. S. R. Channu, R. Holze, and E. H. Walker, *New J. Glas. Ceram.*, 2013, **3**, 29–33.

CHAPTER 3

OXIDE ENTHALPY OF FORMATION AND BAND GAP ENERGY AS ACCURATE DESCRIPTORS OF OXYGEN VACANCY FORMATION ENERGETICS

A paper accepted by *Energy and Environmental Science*

Ann M. Deml,[1,2,†] Vladan Stevanović,[3,4] Christopher L. Muhich,[2] Charles B. Musgrave,[2,5,*] and Ryan O'Hayre[1,*]

[1] Department of Metallurgical and Materials Engineering, Colorado School of Mines, Golden, Colorado 80401, USA
[2] Department of Chemical and Biological Engineering, University of Colorado Boulder, Boulder, Colorado 80303, USA
[3] Department of Physics, Colorado School of Mines, Golden, Colorado 80401, USA
[4] National Renewable Energy Laboratory, Golden, Colorado 80401, USA
[5] Department of Chemistry and Biochemistry, University of Colorado Boulder, Boulder, Colorado 80309, USA
* Corresponding authors
[†] A.M.D. performed the calculations and analysis with the support of V.S. and C.L.M. A.M.D. wrote the manuscript. All authors discussed the data and edited the manuscript.

3.1 Abstract

Despite the fundamental role oxygen vacancy formation energies play in a broad range of important energy applications, their relationships with the intrinsic bulk properties of solid oxides remain elusive. Our study of oxygen vacancy formation in $La_{1-x}Sr_xBO_3$ perovskites (B=Cr, Mn, Fe, Co, and Ni) conducted using modern, electronic structure theory and solid state defect models demonstrates that a combination of two fundamental and intrinsic materials properties, the oxide enthalpy of formation and the minimum band gap energy, accurately correlate with oxygen vacancy formation energies. The energy to form a single, neutral oxygen vacancy decreases with both the oxide enthalpy of formation and the band gap energy in agreement with the relation of the former to metal-oxygen bond strengths and of the latter to the energy of the oxygen vacancy electron redistribution. These findings extend our understanding of the nature of oxygen vacancy formation in complex oxides and provide a fundamental method for predicting oxygen vacancy formation energies using purely intrinsic bulk properties.

3.2 Introduction

A number of important energy applications such as solid oxide fuel cells, oxygen separation membranes, catalytic membrane reactors, and redox oxides for solar fuel cycles depend critically on the participation of oxygen vacancies V_O to mediate the transport of oxygen in a metal oxide. Consequently, these applications would greatly benefit from an improved understanding of V_O formation energetics. Solid oxide fuel cells (SOFCs), for example, offer the exciting possibility of clean and efficient conversion of chemical energy into electricity. Despite intensive research, however, practical implementation of reduced-temperature SOFCs remains limited. A chief challenge is to identify new mixed ion and electron conducting (MIEC) cathode materials offering improved kinetics for the oxygen reduction reaction (ORR). Measured surface oxygen exchange rates have been shown to depend strongly upon the ionic conductivity of the MIEC cathode,[2] which is mediated by oxygen vacancies and thus depends on V_O concentration and mobility. This is consistent with the fact that transport of V_O to oxygen intermediates adsorbed on the oxide surface is often found to be the rate-determining step in MIEC cathodes.[2] As a result, lanthanum strontium transition metal oxide perovskites ($La_{1-x}Sr_xBO_{3-\delta}$) are commonly utilized as cathode materials for intermediate temperature SOFCs due to their high ionic and electronic conductivities and resulting ability to catalyze the ORR. In addition, they exhibit good structural stability, low cost, and moderate thermal expansion.[3,4] Further improvements in SOFC device performance, however, are hindered by the current limited fundamental understanding of V_O formation.

Solar thermochemical (STC) fuel production cycles based on nonstoichiometric[5] or other non-volatile[6] metal oxides also critically depend on oxides with optimally tuned oxygen vacancy formation energies E_V. Thermodynamic studies[7,8] suggest that only oxides with E_V within a certain range are viable for solar H_2O- and CO_2-splitting cycles. Thermodynamic constraints arise because, for maximal efficiency, both redox steps in the STC cycle must be slightly exoergic, that is $\Delta G_{rxn} \approx 0$, but slightly negative. To achieve this requirement, ideal STC oxides must have low to intermediate values of E_V (~1.5-2.5 eV), consistent with the recent[9] discovery that $La_xSr_{1-x}BO_{3-\delta}$ perovskites show great promise for STC applications due to their relatively low and tunable E_V values. Thus, these materials are of great interest to both the SOFC and STC

communities and may find application in other areas that require similar vacancy formation energies. In addition, elucidating the basic principles that govern V_O formation will enable informed optimization of V_O concentrations and accelerate the discovery of new metal oxides for a wide range of applications that critically depend on oxygen vacancies.

The formation of V_O in $LaBO_3$ (LB) perovskites can be expressed (using Kröger-Vink notation) as

$$2B_B^x + O_O^x \rightarrow 2B_B' + V_O^{\cdot\cdot} + \frac{1}{2}O_{2(g)}$$

Here, B_B^x represents the transition metal (TM) B^{3+} ion on its regular lattice site. Removal of neutral oxygen atoms from their regular lattice sites (O_O^x) results in the creation of oxygen vacancies ($V_O^{\cdot\cdot}$) and oxygen molecules. Upon formation of an $V_O^{\cdot\cdot}$, the excess 2 *e* of electronic charge associated with the oxygen atom in the bulk is redistributed to the surrounding lattice. In the case of LB perovskites, this excess electron density primarily localizes on the two neighboring undercoordinated B ions reducing them from a B^{3+} state to an effective B^{2+} (B_B') state.

Sr-substitution of LB perovskites corresponds to

$$SrO + B_B^x \xrightarrow{LaBO_3} Sr_{La}' + B_B^{\cdot}/h^{\cdot} + O_O^x$$

where the presence of Sr^{2+} on La^{3+} sites (Sr_{La}') lowers the electron density donation from the A-site. Charge compensation can be attained via localized oxidation of the TM from B^{3+} to B^{4+} ($B_B^{\cdot}$), creation of delocalized electron holes ($h^{\cdot}$), and/or by decreasing the negative charge on the oxygen ions. The formation of V_O in the LSB perovskites then corresponds to

$$2B_B^{\cdot}/h^{\cdot} + O_O^x \rightarrow 2B_B^x + V_O^{\cdot\cdot} + \frac{1}{2}O_{2(g)}$$

Here, the excess 2 *e* charge previously associated with the removed oxygen atom may reduce the TM back to its original 3+ oxidation state, combine with the delocalized holes, and/or replenish deficient electron density on the remaining oxygen ions.

First principles quantum mechanical methods offer a powerful tool to investigate the fundamental phenomena associated with V_O formation and their composition dependence. Calculations of E_V, electronic structure, and charge distribution in stoichiometric and oxygen deficient structures in particular provide insights into V_O formation energetics, the

corresponding electron density redistribution, and variations due to composition and V_O concentration. Although V_O formation has been studied relatively thoroughly in LB systems for a range of TM B elements, to our knowledge, there have been very few and no extensive studies of V_O formation in Sr-substituted $La_{1-x}Sr_xBO_3$ (LSB) perovskites and no identified unifying principles governing E_V across such systems.

Previous first principles studies of LB compositions have included DFT+U calculations by Pavone *et al.*[10] in which they interpreted trends in E_V to be correlated to TM B-O bond strengths and to exchange energies between the TM *3d* electrons which they estimated from assumed orbital occupations. Although this approach provides valuable insight into the formation of V_O in LB perovskites, the approximate treatment of exchange is not quantitative nor is it applicable as a predictive approach, particularly for systems with high degrees of disproportionation or for metallic systems as occurs in some cases upon Sr-substitution. A detailed DFT+U study of LB systems by Lee *et al.*[11] examined the effects of varying U on E_V and the electronic structure for several LB compositions. Their study convincingly demonstrates the necessity of using non-zero U values to correct self-interaction errors in order to correctly reproduce experimental trends in E_V and calculate more accurate band gap energies. They also show that the trends in the effective Bader charges as a function of the TM B ion are sensitive to the value of U, again demonstrating the importance of using non-zero U values. Lee *et al.*[12] later proposed a correlation between DFT+U E_V and the centroid of the projected density of states (PDOS) of the oxygen *2p* bands relative to the Fermi level, that is the oxygen p-band center, for $LaBO_3$ with B=Mn, Co, and Ni. However, this study deliberately omitted $LaFeO_3$ due to its difference in electronic structure and deviation from the linear trend of Mn, Co, and Ni. Our results confirm that the correlation between E_V and the oxygen p-band center is only generally true and specifically, does not hold for Sr-substituted $LaBO_3$ perovskites. For example, the E_V of $La_{0.6}Sr_{0.4}CrO_3$ is significantly lower than that of $LaCrO_3$ due to critical changes in the oxygen PDOS near the Fermi level. Nevertheless, because the addition of Sr has little effect on the majority of the PDOS, the small change in the oxygen p-band center does not accurately reflect the large decrease in E_V. Only one study by Choi *et al.*[13] has examined E_V in Sr-

substituted lanthanum perovskites; however, the group used only DFT (U=0) which, as demonstrated by Lee *et al.*,[11] is insufficient for these systems.

In this work, the oxygen vacancy formation energies in LB and LSB systems with a range of TM B elements are examined using modern, first principles theories of defects in solids. DFT+U calculations are used along with fitted elemental-phase reference energies (FERE) for accurate compound enthalpies of formation[14,15] $\Delta H_{f,oxide}$. We demonstrate correlations of E_V with $\Delta H_{f,oxide}$ and features of the electronic structure (mainly band gap energy) and explain the observed trends in E_V through analysis of the densities of states. Using these insights, we present a fundamental description of the principles dictating oxygen vacancy formation and provide a new approach for the prediction of oxygen vacancy formation energetics using intrinsic bulk material properties.

3.3 Computational details

Spin polarized DFT+U[16] calculations were performed using a plane wave basis set, the PBE exchange-correlation functional,[17] and the projector augmented wave (PAW) method[18] as implemented in the Vienna Ab-initio Simulation Package (VASP).[19] A Monkhorst-Pack k-point sampling[20] was applied with a constant density corresponding to a 4x4x3 k-point mesh for a 20 atom unit cell resulting in total energies converged within 3 meV/atom with respect to the number of k points. An energy cutoff of 340 eV was used corresponding to a value ~20% greater than the highest suggested by the employed pseudopotentials (282 eV for oxygen). A constant U=3 eV value was used for La and all transition metals in accordance with the U values used for the fitted elemental-phase reference energies (FERE) method developed by Stevanović *et al.*[14] For Sr and O, the Hubbard U parameter was set to zero. This choice of U is also supported by Lee *et al.*'s[11] study where for U=3 eV their calculated trends in E_V reproduce experiment, their mean absolute E_V error decreases from ~0.9 eV for U=0 to ~0.4 eV, and their calculated band gap energies increase for some systems to give improved agreement with experiment compared to U=0. Atomic charges were evaluated using the Bader charge analysis method.[21,22]

Spin degrees of freedom were treated explicitly. At 298 K, the experimental ground state magnetic phases for $LaCrO_3$, $LaMnO_3$, and $LaFeO_3$ are anti-ferromagnetic (AFM) while $LaCoO_3$ and $LaNiO_3$ are paramagnetic.[23] Additionally, most perovskites are paramagnetic at

intermediate to high temperature operating conditions (≥600°C).[24–27] Calculations of truly disordered paramagnetic phases are not feasible within the supercell approach; therefore, a limited search for the DFT+U ground state AFM spin configuration was performed for all LB compositions. Magnetic moments were initialized with high and low spin values and up to eight different AFM configurations within a four formula unit cell. High spin states were obtained for Cr, Mn, Fe, and Co, and low spin states were obtained for Ni. These spin states are consistent with previously calculated[11] and measured[within11] spin states for the LB compositions. The total energy differences between different AFM configurations were typically calculated to be on the order of ~0.01–0.02 eV/atom, consistent with previous studies.[14] The magnitude of these differences indicates that the specific spin configuration does not contribute appreciably to the inherent errors of the DFT method employed in this study. The calculated ground state AFM spin configuration for each LB composition was also used for its corresponding LSB64 composition. Again, different AFM spin configurations are expected to yield negligible differences in the total energies.

All LB compounds were computed from their experimental structures as recorded in the inorganic crystal structure database (ICSD).[28] Both lattice parameters and atomic positions were optimized allowing for lattice distortions. For consistent comparison to available experimental data for LSB compositions with 40% Sr, LSB64 supercells with 37.5% Sr occupation of A sites were generated by random substitution of La with Sr in the ground state 80 atom (16 formula unit) supercells of LB as shown in Figure 3.1 for Cr. At least four A-site cation configurations were calculated for each composition. Structures with an oxygen vacancy were created by removal of a neutral oxygen atom resulting in a nonstoichiometry of δ=0.0625. Only the atomic positions were allowed to relax because structures with relatively low V_O concentrations have similar lattice parameters to structures without V_O such that full relaxation of the lattice has a negligible effect. Introducing Sr lowers the symmetry of the system and creates additional nonequivalent O sites than in the host compound. For this reason, E_V was sampled over at least four randomly chosen oxygen sites for each LSB64 cation configuration. A study of bellybutton configurations will be presented elsewhere.

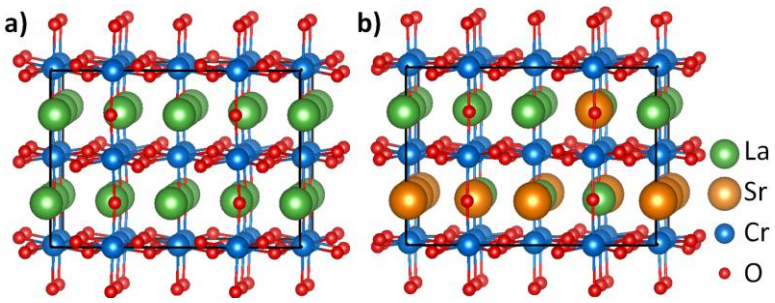

Figure 3.1 Stoichiometric 80 atom supercells of a) $LaCrO_3$ and b) $La_{0.6}Sr_{0.4}CrO_3$ after full relaxation of lattice parameters and ion positions. Several random A-site cation configurations were calculated with multiple oxygen vacancy configurations for each A-site cation configuration.

The formation energy of a neutral oxygen vacancy (hereafter simply referred to as an oxygen vacancy) was calculated according to

$$E_V = E_{tot}^{defect} - E_{tot}^{host} + \mu_O^{FERE}$$

where E_o^{defect} and E_o^{host} are the total energies of the oxygen deficient (defect) and stoichiometric (host) supercells, respectively, and μ_O^{FERE} is the oxygen FERE energy. For those materials exhibiting a band gap, the defect-localized states occur within the gap such that the defects are deep and do not require band gap corrections.[29] Similarly, image charge and potential-alignment corrections were not used[29] due to the explicit charge neutrality of the supercells. Incomplete error cancelation occurs in DFT total energy differences of chemically dissimilar systems such as metals, semiconductors, insulators, and/or gaseous molecules. Alternatively, to correct for errors in the relative energies, the FERE energies, which have been fit to improve calculated standard state enthalpies of formation, were used. Therefore, our predicted E_V values correspond closely to V_O formation energies at 298 K. The calculated values of E_V do not include solid state configurational entropies or thermal corrections due to heat capacity differences between the stoichiometric and oxygen deficient solid state phases, consistent with standard computational approaches[29] for defects in solids. Because these contributions are similar for stoichiometric and oxygen deficient supercells of the same composition, the solid state configurational entropies and thermal corrections at 298 K mostly cancel such that E_V accurately matches V_O formation energies at 298 K.

Oxide enthalpies of formation were also calculated at 298 K using the total energies of the stoichiometric compositions and the FERE energies of the constituent elements where

$$\Delta H_{f,oxide} = E_{tot}^{host} - \sum_i c_i * \mu_i^{FERE}$$

Here, c_i corresponds to the mole fraction of each element present in the stoichiometric compound. Energy differences between the lowest unoccupied state and the highest occupied state ΔE are reported for the stoichiometric compositions. For insulators, ΔE corresponds to the minimum (fundamental) band gap energy E_G. For metals, ΔE is trivially equal to zero. Sr-substituted oxides, however, can possess mid-gap states which result in $\Delta E < E_G$, where E_G is usually associated with the host LB system. Therefore, to remove ambiguity, we discuss our findings in terms of ΔE rather than E_G, and unless otherwise indicated, in this paper our use of the term "band gap" energy more rigorously refers to ΔE.

In this study, LCr denotes $LaCrO_3$, LM=$LaMnO_3$, LF=$LaFeO_3$, LCo=$LaCoO_3$, LN=$LaNiO_3$, LSCr64=$La_{0.6}Sr_{0.4}CrO_3$, LSM64=$La_{0.6}Sr_{0.4}MnO_3$, LSF64=$La_{0.6}Sr_{0.4}FeO_3$, LSCo64=$La_{0.6}Sr_{0.4}CoO_3$, and LSN64=$La_{0.6}Sr_{0.4}NiO_3$. LB, LSB, and LSB64 are used to refer to $LaBO_3$, $La_{1-x}Sr_xBO_3$, and $La_{0.6}Sr_{0.4}BO_3$ compositions, respectively.

3.4 Results and discussion

Herein, we present oxygen vacancy formation energies in LB and LSB systems with a range of TM B elements. We demonstrate correlations of E_V with $\Delta H_{f,oxide}$ and features of the electronic structure (mainly band gap energy) and explain the observed trends in E_V through analysis of the densities of states.

3.4.1 Oxygen vacancy formation energies

Figure 3.2(a) shows calculated oxygen vacancy formation energies E_V for a series of LB and LSB64 compositions with different cation and V_O configurations. Because the standard deviation in E_V between different configurations for each composition is ≤0.2 eV, the average calculated E_V is used for all other analyses. The calculated E_V decrease for the LB compositions such that E_V for B=Cr > Fe > Mn > Co > Ni. Sr-substitution is predicted to significantly lower E_V in all cases but by differing extents such that E_V decreases for the LSB64 compositions with E_V for B=Cr ≈ Mn > Co ≈ Fe ≈ Ni. These results are consistent with experimental thermogravimetric measurements of the oxidation reaction enthalpies for LM,[30] LF,[31] LCo,[32] LSCr64,[33] LSM64,[34]

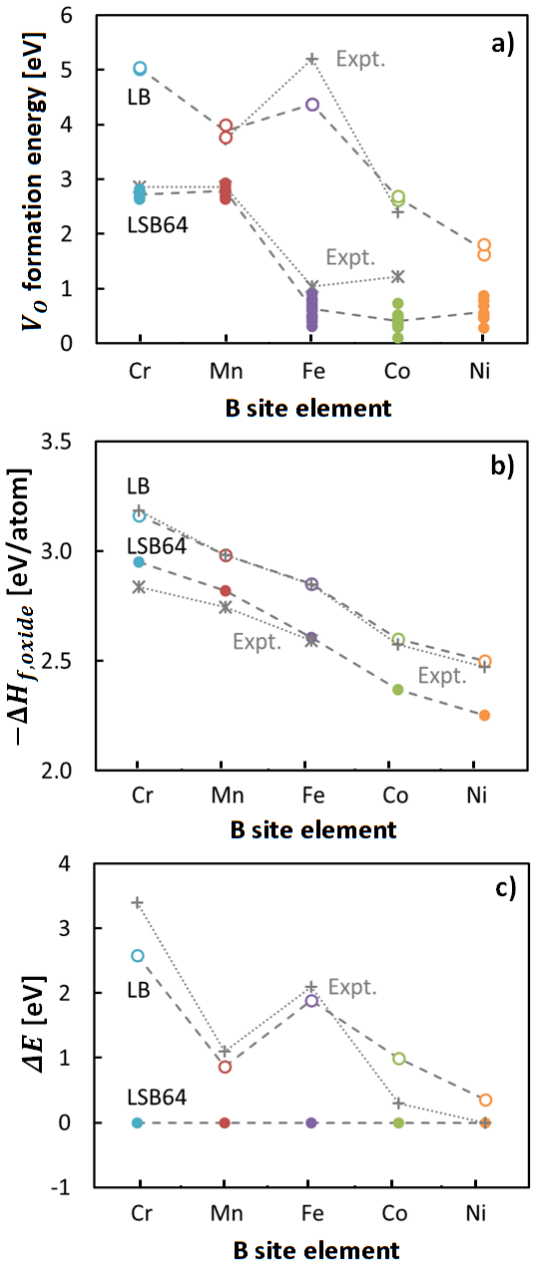

Figure 3.2 DFT+U calculated (○,●) variations in a) oxygen vacancy formation energies, b) oxide enthalpies of formation from their constituent elements, and c) differences between the energies of the lowest unoccupied state and highest occupied state ΔE for $LaBO_3$ (LB) and $La_{0.6}Sr_{0.4}BO_3$ (LSB) compositions where B=Cr, Mn, Fe, Co, and Ni. Oxide enthalpy of formation serves as an indicator of average bond strength, and ΔE corresponds to the minimum band gap energy for insulators. LB compositions are mostly insulators while LSB64 compositions are degenerate semiconductors (with defect states near E_{HOS}) or metallic oxides. Multiple data points for a given composition in a) refer to different cation and oxygen vacancy configurations while b) and c) show only average values. References for experimental data (+,∗) are provided in the text.

LSF64,[31] and LSCo64[32] where the oxidation reaction enthalpy of LSCr64 was extrapolated from lower Sr-concentrations. Additional information regarding the selection of experimental data is provided in Appendix B. The above trends in calculated E_V across the LB compositions are also consistent with previously reported E_V calculated for $LaBO_3$ (B=Cr, Mn, Fe, and Co) using DFT+U[10,11] and HSE.[10]

3.4.2 E_V correlations with oxide enthalpy of formation and electronic structure

We now consider two material properties: i) oxide enthalpies of formation and ii) band gap energies, which are calculated as the energy differences between the lowest unoccupied state and the highest occupied state. As described below, we find that oxide enthalpies of formation are related to metal-oxygen bond strengths and band gap energies are related to the energy of the V_O electron density redistribution. As a result, a combination of these two properties accurately correlates with calculated E_V for these LB and LSB64 systems.

Calculated enthalpies of formation of the oxides from their constituent elements $\Delta H_{f,oxide}$ (Figure 3.2(b)) serve as an indicator of the average metal-oxygen bond strength. Within the LB compositions, the consistent crystal structure gives rise to approximately constant La-O interactions (our calculated average charges on La vary by ≤ 0.02 *e*) such that differences in bond strengths occur primarily due to differences in bonding with the B-site atom. In other words, changing the identity of the B-site atom affects only the bond energy of the B-O bond and is expected to have little influence on the La-O bond strengths. The same holds true within the LSB64 compositions where the average A-site interactions with oxygen remain unchanged with changes in the B-site atom as indicated by the ≤ 0.02 *e* variation in the average charges on La and Sr. As a result, decreasing $-\Delta H_{f,oxide}$ within the LB and LSB64 systems indicates decreasing B-O bond strength relative to the metallic B-B bonds in the order $-\Delta H_{f,oxide}$ for B=Cr > Mn > Fe > Co > Ni.

In contrast to the trends in E_V, our calculations show that Sr-substitution lowers $-\Delta H_{f,oxide}$ by an approximately constant magnitude of 0.20-0.25 eV for all B indicating a consistent decrease in the average bond strength. The relative contributions from A-O, B-O, and A-B interactions to this decrease can be inferred using the observation that the experimental formation energies of ABO_3 and BO_2 differ by a constant value for different A and B cations.[35]

This consistent difference in formation energies indicates that it results primarily from the added A-site interactions, which in the case of LB and LSB64 compositions, corresponds to changes in the A-O bonds. Therefore, we conclude that La-O bonds are stronger than Sr-O bonds such that the A-O bond strength decreases as a result of Sr-substitution. This is also consistent with the expected decrease in electrostatic attraction between the O^{2-} anions and the Sr^{2+} versus La^{3+} cations.

The $\Delta H_{f,oxide}$ calculated from FERE elemental energies are in good agreement with experimentally measured values for the LB[36,37] compositions, LSCr64,[38] LSM64,[39] and LSF64.[40] The experimental $\Delta H_{f,oxide}$ for LSCr64 and LSF64 were calculated from enthalpies of formation from oxides, and experimental $\Delta H_{f,oxide}$ for LSCr64 and LSM64 were extrapolated and interpolated from other Sr-concentrations, respectively. Additional information regarding the experimental data is provided in Appendix B. In addition, our calculated trend of decreasing $-\Delta H_{f,oxide}$ with increasing atomic number of B is consistent with previous studies[35,41,42] in which the decrease is attributed to the energy decrease of the TM *3d* band with increasing atomic number of B. Our results do not, however, support the further claim by Zeng *et al.*[35] that this trend is attributable to a steady increase in B-O bond covalency and a corresponding decrease in charge on the TM B cations. Instead, our Bader atomic charges (Figure B1) exhibit a nonlinear trend with respect to the atomic number of B and indicate that Mn exhibits the weakest B-O bond covalency of this set.

In general, decreased bond strength, as indicated by less negative $\Delta H_{f,oxide}$, tends to correlate with decreased E_V as shown in Figures 3.2(b) and 3.2(c). This correlation is consistent with the expectation that weaker bonds make removal of oxygen atoms more facile. However, there exist significant deviations within this trend. To account for these deviations, the electronic structure is considered.

Redistribution of the excess electron density due to V_O formation fills previously unoccupied states; as a result, a higher energy state becomes the highest occupied state and the corresponding energy of the highest occupied state E_{HOS} increases. The total densities of states (TDOS) for stoichiometric and oxygen deficient LB and LSB64 compositions (Figure B.2) show that the magnitude of the increase in E_{HOS} roughly trends with the magnitude of the

energy difference between the lowest unoccupied state and the highest occupied state ΔE. Thus, a smaller ΔE results in a lower energy V_O-induced defect band and decreases E_V.

The considered LB compositions are electronic insulators (with the exception of LN) and exhibit decreasing ΔE in the order ΔE for B=Cr > Fe > Mn ≈ Co > Ni (Figure 3.2(c)). We note here that our calculations give a small (<0.4 eV), nonzero ΔE for LN which is otherwise observed to be a correlated metal.[43] A slightly smaller value of U would likely close this gap; however, for consistency and due to the low calculated density of states at E_{HOS} for LN, we have treated it in a manner consistent with insulators and degenerate semiconductors. Comparison of our calculated ΔE with measured optical band gaps[43] for the LB compositions gives good agreement as shown in Figure 3.2(c).

In contrast, the LSB64 compositions we considered are degenerate semiconductors (semiconductors that have begun to exhibit metallic electronic character due to the high level of doping) or metallic oxides. Therefore, ΔE is negligible in these cases because degenerate semiconductors exhibit unoccupied defect band energies near or at E_{HOS} and metals exhibit a high density of states at E_{HOS} (which is then equivalent to the Fermi energy E_F). The E_{HOS} increase due to V_O formation is also significantly smaller for the Sr-substituted lanthanum perovskites than for those without Sr-substitution. The negligible ΔE in LSB64 compositions significantly lowers E_V, as is particularly evident in those systems exhibiting metallic character. This is consistent with experimental observations of moderate to high electronic conductivity in LSCr,[44] LSM,[45] LSF,[46] and LSCo.[47]

A linear combination of $\Delta H_{f,oxide}$ and ΔE accurately predicts E_V as shown in Figures 3.3(a) and 3.3(b) for calculated and measured $\Delta H_{f,oxide}$ and ΔE, respectively. This correlation exhibits two regimes: the first consisting of insulators and semiconductors and the second consisting of metallic oxides. Insulators and semiconductors exhibit decreasing E_V with decreasing $-\Delta H_{f,oxide}$ and decreasing ΔE. The line that best describes this relationship for calculated $\Delta H_{f,oxide}$ and ΔE is given by

$$E_V = 2.74\left[-\Delta H_{f,oxide}^{FERE} + 0.26 * \Delta E^{DFT+U}\right] - 5.12$$

where the constants (the y-intercept and the relative contributions from $\Delta H_{f,oxide}$ and ΔE) were obtained by linear regression and the units of $\Delta H_{f,oxide}$ and ΔE are eV/atom and eV, respectively. For measured $\Delta H_{f,oxide}$ and ΔE, the best linear fit is given by

$$E_V = 2.09\left[-\Delta H_{f,oxide}^{expt} + 0.25 * \Delta E^{expt}\right] - 3.06$$

This combined $\Delta H_{f,oxide}$ and ΔE descriptor gives a significantly improved correlation with E_V as compared to either of the individual parameters alone (Figure B.3) as shown by increasing R^2 values of 0.67, 0.72, and 0.94 for linear regression fits for only $\Delta H_{f,oxide}$, only ΔE, and for the combined parameter, respectively. All seven non-metallic LB and LSB64 compositions were

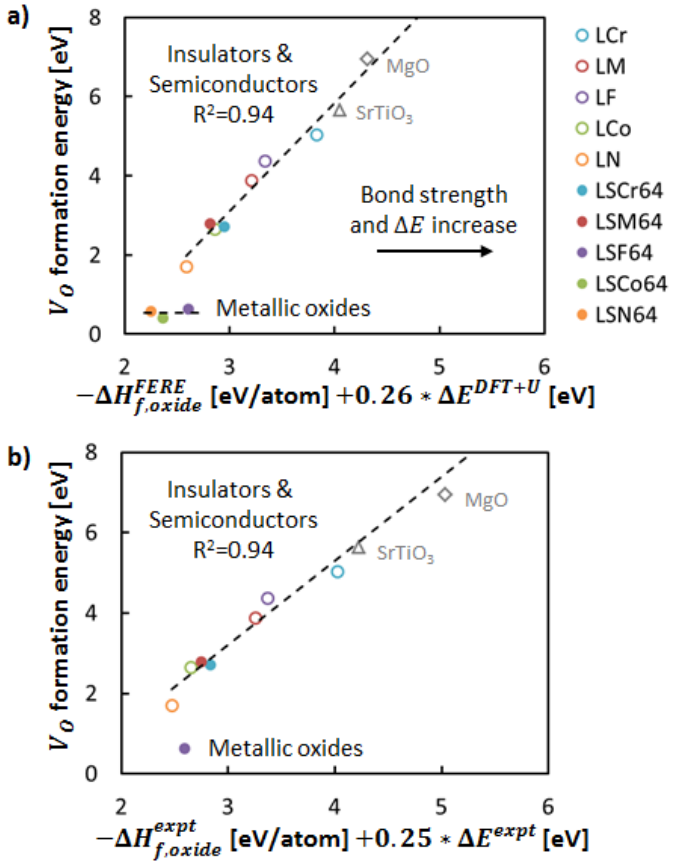

Figure 3.3 Oxygen vacancy formation energies for LB and LSB64 compositions as a function of a linear combination of a) calculated and b) experimental oxide enthalpies of formation $\Delta H_{f,oxide}$ and band gap energies calculated as the difference between the energies of the lowest unoccupied state and the highest occupied state ΔE. Two different regimes are predicted corresponding to i) insulators and semiconductors and ii) metallic oxides. Only nonmetallic LB and LSB64 compositions were used in the fits, although the lines are extended for comparison with MgO and $SrTiO_3$. References for experimental data are provided in the text.

used for these fits; however, the strategy of leave-one-out cross-validation (e.g. omitting Ni-containing compositions for later validation of the fit) does not yield any significant changes.

The transition from semiconducting to metallic oxides introduces a discontinuity in this trend resulting in significantly lower E_V (< 1 eV) for the metallic oxides LSF64, LSCo64, and LSN64. The small E_V observed for metallic oxides appears to be independent of $\Delta H_{f,oxide}$ and ΔE and likely results from the extensive delocalization of excess V_O charge density in these materials. Further studies are required to extend our model by means of an alternative or more broadly applicable descriptor of E_V that applies for metallic oxides.

The same analysis was also applied to two additional oxide compositions, $SrTiO_3$ and MgO, which exhibit perovskite and rock-salt crystal structures, respectively. These two nonmagnetic compounds were chosen for their computational simplicity and for the availability of experimental data.[48–50] As shown in Figure 3.3, the calculated E_V for both MgO and $SrTiO_3$ agree well with fits from the nonmetallic LB and LSB64 compositions indicating that our approach for predicting E_V from $\Delta H_{f,oxide}$ and ΔE may be more broadly applicable to other metal oxides.

We emphasize the convenience and value of this predictive correlation between E_V, $\Delta H_{f,oxide}$, and ΔE by calling attention to the fact that both calculated and experimental values provide accurate correlations. Furthermore, the calculated $\Delta H_{f,oxide}$ and ΔE can be obtained from calculations of bulk stoichiometric phases. Our approach, therefore, altogether avoids the more costly and time consuming relaxation and total energy calculations of oxygen vacancy-containing cells, providing a tool for rapid screening of oxygen vacancy formation energetics. We note that the specific values for the relationship between E_V, $\Delta H_{f,oxide}^{FERE}$, and ΔE^{DFT+U} are all calculated using a specific choice of DFT functional (PBE), Hubbard correction (U=3 eV), k-point grid (Monkhorst-Pack) and density, and supercell size (80 atoms). Different computational choices will result in a different linear relationship, although the trend is expected to be robust as demonstrated by the experimental data (Figure 3.3(b)). Similar linear relationships are expected to exist between these materials properties calculated using different levels of theory as long as the methods correctly describe the energetics of TM-O bond dissociation and the electronic structure (ΔE). Consequently, for the purposes of understanding oxygen vacancy

formation energetics and identifying promising metal oxides with desirable E_V, highly accurate but computationally expensive electronic structure methods, such as the GW quasiparticle methods, are unnecessary and impractical.

3.4.3 Densities of states

Having established a practical and convenient approach for the prediction of E_V from $\Delta H_{f,oxide}$ and ΔE, we now discuss the origin of this relationship through a more detailed examination of the electronic structure.

The total (TDOS) and projected densities of states (PDOS) for stoichiometric LB and LSB64 compositions in Figure 3.4 illustrate the effect of Sr-substitution on electronic structure. Different cation configurations result in slight variations in the LSB64 DOS, but characteristic features remained consistent. Substitution of Sr^{2+} on La^{3+} sites (Sr'_{La}) decreases the electronic charge donation from the A-site, and charge compensation can be attained via:

i) Localized oxidation of the TM from B^{3+} to B^{4+} ($B_B^{\cdot}$) to produce mid-gap defect bands as observed for LSCr64 and LSM64,

ii) Creation of delocalized electron holes ($h^{\cdot}$) to produce a partially filled conduction band as observed for LSF64, LSCo64, and LSN64, and/or

iii) Lowering of the negative charge on oxygen ions as observed to some extent for all compositions (Figure B.1).

The partial covalent nature of the TM B-O bonds,[51–53] and the resulting ability of O to participate in charge accommodation, is evidenced by the overlap of the TM *3d* and O *2p* PDOS and by the significant difference between the effective charges on B and O ions and their formal oxidation states (Figure B.1).

The removal of charge from hybridized TM *3d*-O *2p* states shifts these states to higher energies (above the energy of the highest occupied state E_{HOS}) such that with Sr-substitution all systems considered here exhibit unoccupied states of TM *3d*-O *2p* character at or immediately above E_{HOS}. These states more readily accept electron density upon V_O formation and thereby lower E_V as previously discussed. Compositions exhibiting localized defect states and a low TDOS at E_{HOS} (LSCr64 and LSM64) are considered to be degenerate semiconductors while those with a partially filled conduction band and high TDOS at $E_{HOS} = E_F$ (LSF64, LSCo64,

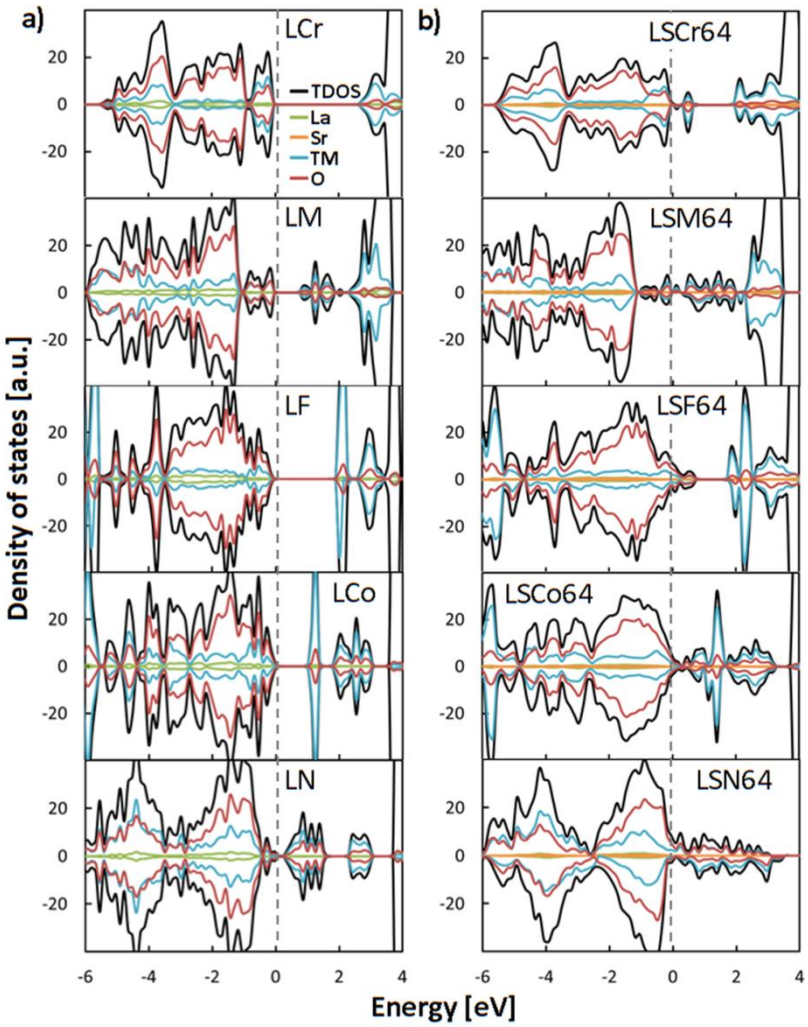

Figure 3.4 Total and partial densities of states (DOS) for stoichiometric a) LB compositions commonly show insulating properties which result in moderate to high oxygen vacancy formation energies while b) LSB64 compositions exhibit low energy unoccupied states of TM *3d*-O *2p* character which significantly lower oxygen vacancy formation energies. The energy of the highest occupied state is aligned to zero. Spin-up and spin-down DOS are shown as positive and negative values, respectively.

and LSN64) are considered to be metallic oxides. These results are consistent with experimental observations of p-type electronic transport by small polaron hopping for LSCr[44] and LSM[45] and by delocalized metallic conductivity in LSCo.[47,54] LSF, on the other hand, is widely reported[55,56] to exhibit a small polaron hopping mechanism; however, recent work[46] has noted that LSF does not show the thermal activation expected for small polaron hopping. Therefore, the nature of electronic transport in LSF is less certain.

The calculated gaps in the TDOS at ~0.7 eV above E_{HOS} for both LSCr64 and LSF64 are consistent with the experimentally observed LSCr[33] and LSF[57] plateaus in oxygen nonstoichiometry as a function of oxygen partial pressure for the Cr^{3+} and Fe^{3+} oxidation states. As V_O concentrations increase in these systems, the excess electronic charge created by V_O formation fills the empty TM B-O bonding states near E_{HOS}. However, these lower energy states (corresponding to B^{4+}, $h^{\cdot}$, and/or decreased charge on oxygen sites) reach full occupancy as the average TM B oxidation state approaches 3+ thereby requiring higher energy (lower oxygen partial pressure) to further reduce the oxide and create additional V_O. In contrast, LSM64, LSCo64, and LSN64 do not exhibit such a gap in the TDOS above E_{HOS}, which allows for a smooth reduction from B^{4+} to B^{2+} consistent with experimental observations of no plateau in the oxygen nonstoichiometry for LSM[58] and LSCo.[32]

Visualization of the electron density redistribution upon V_O formation further illustrates the changes in electronic structure with Sr-substitution. As previously discussed, in LB compositions the excess electron density due to V_O formation is typically localized on the nearest neighbor TM B ions as shown in Figures 3.5(a) and 3.5(b). Sr-substitution, however, produces low energy unoccupied TM *3d*-O *2p* states throughout the structure which readily

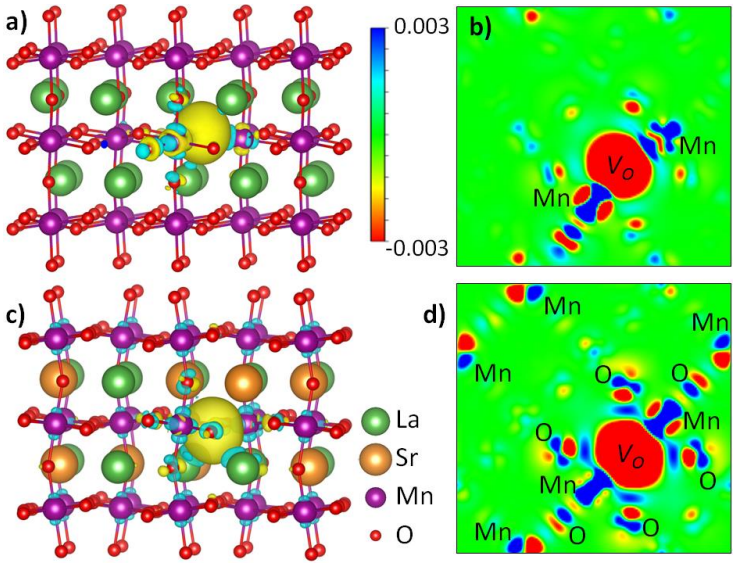

Figure 3.5 Changes in electron density (e/Å^3) upon V_O formation in LM (a,b) and LSM64 (c,d). 3D isosurfaces (a,c) and 2D contour maps of the V_O (001) plane (b,d) show increased participation of TM B and O ions in accommodating excess electron density resulting from V_O with Sr-substitution. Yellow isosurfaces indicate lowered electron density; cyan indicates increased electron density.

accept the excess electron density made available on formation of V_O, distributing it beyond the V_O nearest neighbors (Figure 3.5(c) and 3.5(d)). The partial covalent nature of the TM B-O bonds is evidenced by the participation of both TM B and O ions in the V_O charge accommodation. Similar behavior is observed for each of the considered LB compositions. The corresponding TDOS for the stoichiometric and oxygen deficient LB and LSB compositions (previously discussed) are provided in Figure B.2.

3.4.4 Extensions

Our calculated E_V and TDOS are consistent with the widespread use of LSB and further substituted perovskites for intermediate temperature SOFC cathodes. These results explain the high electronic and ionic conductivities of these systems through the ease of V_O formation and the availability of states at or immediately above E_{HOS}. For example, measured conductivities of LSCr64,[44] LSM64,[45] LSF64,[46] and LSCo64[47] show that LSCo64 exhibits the highest electronic conductivity of this set, consistent with its low E_V. The electronic conductivity of LSF64 is decreased as a result of the Fe^{3+} plateau. The mixed ionic-electronic conducting nature of LSB perovskites is also commonly utilized in oxygen separation membranes where oxygen ions and electronic charge are transported in opposite directions for a net effective transport of oxygen gas. The rates of oxygen permeation in $La_{0.6}Sr_{0.4}Co_{0.8}B'_{0.2}O_{3-\delta}$ are similar for B'=Mn, Cr, and Fe but increase significantly for Co and Ni,[59] which is again consistent with the low E_V in LSCo64 and LSN64 and the Fe^{3+} plateau in LSF64.

We recommend the design of additional perovskite compositions with A and B-site substitutions and target oxygen vacancy energetics through consideration of the bond strengths and electronic structures of their constituent oxides. For example, the intermediate bond strength as measured by $-\Delta H_{f,oxide}$ and localized charge properties of LSCr and/or LSM may be combined with the low bond strength and metallic nature of LSCo and/or LSN via co-doping to tune E_V and attain an optimal value for STC fuel production cycles. This strategy provides for efficient, informed discovery of novel systems with improved performance and has frequently been effective in optimizing other properties of perovskites such as stability, ionic and electronic conductivity, and catalytic behavior.

Furthermore, our approach for predicting E_V from $\Delta H_{f,oxide}$ and ΔE may be more broadly applicable to other oxide structures and even non-oxides. Also consistent with our results, related studies[60,61] of binary oxides such as BaO, CaO, MgO, and SrO have reported E_V to be proportional to the band gap energy for systems with V_O-induced localized defect states. Tanaka *et al.*[61] also reported low E_V for binary oxide systems with metallic character and observed a similar E_V dependency on the band gap energy in nitrides. As such, the potential applicability of this approach for rapidly screening E_V in a broad range of material systems is promising, and demonstration of its applicability to a wider variety of materials is ongoing. Preliminary results indicate that this model applies to a wide range of oxide compositions and crystal structures although the specific linear relationship between E_V, $\Delta H_{f,oxide}$, and ΔE may differ between different classes of oxides, which could lead to a decrease in the overall degree of correlation for any single fit (to be presented elsewhere).

3.5 Conclusions

We have presented a fundamental description of oxygen vacancy V_O formation as well as an efficient, new approach for the prediction of oxygen vacancy formation energies E_V. Furthermore, these detailed insights into V_O formation and our new approach for predicting E_V enable the development of a deeper understanding of oxygen vacancy formation energetics which can also aid in accelerating the discovery of new materials that rely on oxygen vacancies for their desirable properties. Our computational study of $La_{1-x}Sr_xBO_3$ perovskites shows that E_V decreases with bond strength, as inversely indicated by the oxide enthalpy of formation $\Delta H_{f,oxide}$, and with the energy difference between the lowest unoccupied state and the highest occupied state ΔE. Together these two intrinsic materials properties provide a good correlation to E_V with regimes consisting of i) insulators and semiconductors and ii) metallic oxides. A discontinuity between these two regimes results in significantly lower E_V for metallic oxides.

We explain this correlation via detailed analysis of the electronic structure of stoichiometric and oxygen deficient structures. The lower E_V that results from decreased $-\Delta H_{f,oxide}$ is consistent with the expectation that weaker bonds result in increased ease of oxygen removal. In addition, the LB and LSB64 densities of states show that the increase in the energy of the highest occupied state E_{HOS} due to V_O formation generally trends with the

magnitude of ΔE. As such, Sr-substitution of LB compositions results in the lowering of E_V due to the creation of unoccupied states at or near E_{HOS}. These states are readily populated by the excess electron density arising from V_O formation to give low E_V.

We propose that novel perovskite compositions may be designed for target E_V properties using this approach to consider the bond strengths and electronic structures of their constituent oxides. Furthermore, although we have demonstrated this analysis and new approach within the $La_{1-x}Sr_xBO_3$ perovskite family, because our approach is based on the fundamental phenomena dictating vacancy formation, it is likely applicable to a range of other material systems including other oxides and potentially even non-oxide systems.

3.6 Acknowledgements

This research was supported by the National Science Foundation (NSF) through the Renewable Energy Materials Research Science and Engineering Center (REMRSEC) under Grant No. DMR-0820518 and from the Department of Energy Office of Science Graduate Fellowship Program (DOE SCGF), made possible in part by the American Recovery and Reinvestment Act of 2009, administered by ORISE-ORAU under contract no. DE-AC05-06OR23100. V.S. acknowledges support from the National Science Foundation under Grant No. DMR-1309980. This work utilized the Janus supercomputer, which is supported by the NSF (award number CNS-0821794) and the University of Colorado Boulder. The Janus supercomputer is a joint effort of the University of Colorado Boulder, the University of Colorado Denver, and the National Center for Atmospheric Research. The authors thank J. Tong and A. Holder for valuable discussions and suggestions. C.B.M. is a Fellow of the Materials Science Program and the Renewable and Sustainable Energy Institute of the University of Colorado Boulder and the National Renewable Energy Laboratory.

3.7 References

1. H. Peng, D. O. Scanlon, V. Stevanović, J. Vidal, G. W. Watson, and S. Lany, *Phys. Rev. B*, 2013, **88**, 115201.
2. L. Wang, R. Merkle, Y. A. Mastrikov, E. A. Kotomin, and J. Maier, *J. Mater. Res.*, 2012, **27**, 2000–2008.
3. S. B. Adler, *Chem. Rev.*, 2004, **104**, 4791–4843.
4. S. Stølen, E. Bakken, and C. E. Mohn, *Phys. Chem. Chem. Phys.*, 2006, **8**, 429–447.

5. W. C. Chueh, C. Falter, M. Abbott, D. Scipio, P. Furler, S. M. Haile, and A. Steinfeld, *Science*, 2010, **330**, 1797–1801.

6. C. L. Muhich, B. W. Evanko, K. C. Weston, P. Lichty, X. Liang, J. Martinek, C. B. Musgrave, and A. W. Weimer, *Science*, 2013, **341**, 540–542.

7. I. Ermanoski, N. P. Siegel, and E. B. Stechel, *J. Sol. Energy Eng.*, 2013, **135**, 031002.

8. B. Meredig and C. Wolverton, *Phys. Rev. B*, 2009, **80**, 245119.

9. A. H. McDaniel, E. C. Miller, D. Arifin, A. Ambrosini, E. N. Coker, R. O'Hayre, W. C. Chueh, and J. Tong, *Energy Environ. Sci.*, 2013, **6**, 2424–2428.

10. M. Pavone, A. M. Ritzmann, and E. A. Carter, *Energy Environ. Sci.*, 2011, **4**, 4933–4937.

11. Y.-L. Lee, J. Kleis, J. Rossmeisl, and D. Morgan, *Phys. Rev. B*, 2009, **80**, 224101.

12. Y. Lee, J. Kleis, J. Rossmeisl, Y. Shao-Horn, and D. Morgan, *Energy Environ. Sci.*, 2011, **4**, 3966.

13. Y. Choi, M. C. Lin, and M. Liu, *J. Power Sources*, 2010, **195**, 1441–1445.

14. V. Stevanović, S. Lany, X. Zhang, and A. Zunger, *Phys. Rev. B*, 2012, **85**, 115104.

15. S. Lany, *Phys. Rev. B*, 2008, **78**, 245207.

16. S. L. Dudarev, G. A. Botton, S. Y. Savrasov, C. J. Humphreys, and A. P. Sutton, *Phys. Rev. B*, 1998, **57**, 1505–1509.

17. J. P. Perdew, K. Burke, and M. Ernzerhof, *Phys. Rev. Lett.*, 1996, **77**, 3865–3868.

18. P. Blöchl, *Phys. Rev. B*, 1994, **50**, 17953–17979.

19. G. Kresse and J. Furthmüller, *Comput. Mater. Sci.*, 1996, **6**, 15–50.

20. H. Monkhorst and J. Pack, *Phys. Rev. B*, 1976, **13**, 5188–5192.

21. G. Henkelman, A. Arnaldsson, and H. Jónsson, *Comput. Mater. Sci.*, 2006, **36**, 354–360.

22. R. F. W. Bader, *Atoms in Molecules: A Quantum Theory*, Oxford University Press, Oxford, 1990.

23. Z. Yang, Z. Huang, L. Ye, and X. Xie, *Physcial Rev. B*, 1999, **60**, 15674.

24. Y. Urishabara, A. Moritomo, Y. Arima, T. Asatmisu, and A. Kido, *Phys. Rew. B*, 1995, **51**, 103–109.

25. W. C. Koehler and E. O. Wollan, *J. Phys. Chem. Solids*, 1957, **2**, 100–106.

26. K. Tezuka, Y. Hinatsu, A. Nakamura, T. Inami, Y. Shimojo, and M. Y, *J. Solid State Chem.*, 1998, **141**, 404–410.

27. A. Wattiaux, J. C. Grenier, M. Pouchard, and P. Hagenmuller, *J. Electrochem. Soc.*, 1987, **134**, 1718–1724.

28. A. Belsky, M. Hellenbrandt, V. L. Karen, and P. Luksch, *Acta Crystallogr. Sect. B Struct. Sci.*, 2002, **B58**, 364–369.

29. S. Lany and A. Zunger, *Phys. Rev. B*, 2008, **78**, 235104.

30. J. H. Kuo, H. U. Anderson, and D. M. Sparlin, *J. Solid State Chem.*, 1989, **83**, 52–60.

31. J. Mizusaki, M. Yoshihiro, S. Yamauchi, and K. Fueki, *J. Solid State Chem.*, 1987, **67**, 1–8.

32. J. Mizusaki, Y. Mima, S. Yamauchi, K. Fueki, and H. Tagawa, *J. Solid State Chem.*, 1989, **80**, 102–111.

33. J. Mizusaki, S. Yamauchi, K. Fueki, and A. Ishikawa, *Solid State Ionics*, 1984, **12**, 119–124.

34. J. Mizusaki, H. Tagawa, K. Naraya, and T. Sasamoto, *Solid State Ionics*, 1991, **49**, 111–118.

35. Z. Zeng, F. Calle-Vallejo, M. B. Mogensen, and J. Rossmeisl, *Phys. Chem. Chem. Phys.*, 2013, **15**, 7526–7533.

36. J. Cheng and A. Navrotsky, *J. Mater. Res.*, 2003, **18**, 2501–2508.

37. K. T. Jacob and M. Attaluri, *J. Mater. Chem.*, 2003, **13**, 934–942.

38. J. Cheng and A. Navrotsky, *J. Solid State Chem.*, 2005, **178**, 234–244.

39. C. Laberty, A. Navrotsky, C. N. R. Rao, and P. Alphonse, *J. Solid State Chem.*, 1999, **145**, 77–87.

40. J. Cheng, A. Navrotsky, X. Zhou, and H. U. Anderson, *Chem. Mater.*, 2005, **17**, 2197–2207.

41. F. Calle-Vallejo, J. I. Martínez, J. M. García-Lastra, M. Mogensen, and J. Rossmeisl, *Angew. Chemie*, 2010, **49**, 7699–7701.

42. J. I. Martínez, H. A. Hansen, J. Rossmeisl, and J. K. Nørskov, *Phys. Rev. B*, 2009, **79**, 045120.

43. T. Arima, Y. Tokura, and J. B. Torrance, *Phys. Rev. B*, 1993, **48**, 17006–17009.

44. D. P. Karim and A. T. Aldred, *Phys. Rev. B*, 1979, **20**, 2255–2263.

45. J. Mizusaki, Y. Yonemura, H. Kamata, K. Ohyama, N. Mori, H. Takai, H. Tagawa, M. Dokiya, K. Naraya, T. Sasamoto, H. Inaba, and T. Hashimoto, *Solid State Ionics*, 2000, **132**, 167–180.

46. M. Søgaard, P. V. Hendriksen, and M. Mogensen, *J. Solid State Chem.*, 2007, **180**, 1489–1503.

47. M. Søgaard, P. V Hendriksen, M. Mogensen, F. W. Poulsen, and E. Skou, *Solid State Ionics*, 2006, **177**, 3285–3296.

48. R. C. Whited, C. J. Flaten, and W. C. Walker, *Solid State Commun.*, 1973, **13**, 1903–1905.

49. K. van Benthem, C. Elsässer, and R. H. French, *J. Appl. Phys.*, 2001, **90**, 6156–6164.

50. D. D. Wagman, W. H. Evans, V. B. Parker, R. H. Schumm, I. Halow, S. M. Bailey, K. L. Churney, and R. L. Nuttall, *J. Phys. Chem. Ref. Data*, 1982, **11**, Supplement No. 2.

51. M. M. Kuklja, E. A. Kotomin, R. Merkle, Y. A. Mastrikov, and J. Maier, *Phys. Chem. Chem. Phys.*, 2013, **15**, 5443–5471.

52. J. He and C. Franchini, *Phys. Rev. B*, 2012, **86**, 235117.

53. J. Suntivich, H. a Gasteiger, N. Yabuuchi, H. Nakanishi, J. B. Goodenough, and Y. Shao-Horn, *Nat. Chem.*, 2011, **3**, 546–550.

54. M. H. R. Lankhorst, H. J. M. Bouwmeester, and H. Verweij, *J. Solid State Chem.*, 1997, **133**, 555–567.

55. J. Mizusaki, T. Sasamoto, W. R. Cannon, and H. K. Bowen, *J. Am. Ceram. Soc.*, 1983, **66**, 247–252.

56. M. V. Patrakeev, I. A. Leonidov, V. L. Kozhevnikov, and K. R. Poeppelmeier, *J. Solid State Chem.*, 2005, **178**, 921–927.

57. J. Mizusaki, M. Yoshihiro, S. Yamauchi, and K. Fueki, *J. Solid State Chem.*, 1985, **58**, 257–266.

58. J. Mizusaki, N. Mori, H. Takai, Y. Yonemura, H. Minamiue, H. Tagawa, M. Dokiya, H. Inaba, K. Naraya, T. Sasamoto, and T. Hashimoto, *Solid State Ionics*, 2000, **129**, 163–177.

59. Y. Teraoka, T. Nobunaga, and N. Yamazoe, *Chem. Lett.*, 1988, 503–506.

60. T. Yamamoto and T. Mizoguchi, *Ceram. Int.*, 2013, **39**, S287–S292.

61. I. Tanaka, K. Tatsumi, M. Nakano, H. Adachi, and F. Oba, *J. Am. Ceram. Soc.*, 2002, **85**, 68–74.

62. E. A. Kotomin, Y. A. Mastrikov, M. M. Kuklja, R. Merkle, A. Roytburd, and J. Maier, *Solid State Ionics*, 2011, **188**, 1–5.

CHAPTER 4

UNIFYING DESCRIPTORS OF OXYGEN VACANCY FORMATION ENERGIES ACROSS A BROAD RANGE OF OXIDE COMPOSITIONS AND STRUCTURES

A paper in preparation

Ann M. Deml,[1,2,†] Aaron M. Holder,[2,3] Ryan O'Hayre,[1] Charles B. Musgrave,[2,3] and Vladan Stevanović,[4,5,*]

[1] Department of Metallurgical and Materials Engineering, Colorado School of Mines, Golden, Colorado 80401, USA
[2] Department of Chemical and Biological Engineering, University of Colorado Boulder, Boulder, Colorado 80303, USA
[3] Department of Chemistry and Biochemistry, University of Colorado Boulder, Boulder, Colorado 80309, USA
[4] Department of Physics, Colorado School of Mines, Golden, Colorado 80401, USA
[5] National Renewable Energy Laboratory, Golden, Colorado 80401, USA
* Corresponding author
[†] A.M.D. performed the calculations and analysis with the support of V.S. and A.M.H. A.M.D. wrote the manuscript. All authors discussed the data and edited the manuscript.

4.1 Abstract

A broad range of important energy applications depend critically on the participation of oxygen vacancies; however, fundamental understanding of the relationships between oxygen vacancy formation energies E_V and the intrinsic bulk properties of oxides remains incomplete. We examine a broad range of oxide compounds with perovskite, antifluorite, corundum, rock salt, and rutile crystal structures and identify two simple, easily predicted descriptors of E_V. For small band gap perovskites, a combination of the oxide enthalpy of formation and the energy of the lowest unoccupied state relative to the O *2p* band center accurately correlate with E_V. For larger band gap oxides, a combination of the oxide enthalpy of formation and the minimum band gap energy correlate with E_V. In both cases, the first term relates to the metal-oxygen bond strengths and the second relates to the energetic redistribution of the oxygen vacancy electrons. These findings extend our understanding of the dominant physical mechanisms contributing to E_V in oxides and provide a valuable method for efficiently predicting E_V from intrinsic bulk properties.

4.2 Introduction

Many notable energy applications such as solid oxide fuel cells, oxygen separation membranes, catalytic membrane reactors, and redox oxides for solar fuel cycles contain metal oxide components whose performance depends critically on the participation of oxygen vacancies V_O. Although modern theoretical tools can accurately compute oxygen vacancy formation energetics,[1] a broader understanding of the relationship between oxygen vacancy formation energies E_V and the intrinsic bulk properties of oxides is just developing.[2–5] As a result, the ability to design new redox active materials with desirable oxygen vacancy formation thermodynamics remains a challenge.

Although a few studies have examined the material dependence of E_V within relatively small groups of similar oxides, to our knowledge, a fundamental and unifying set of E_V descriptors that applies across broad variations in composition including different crystal structures has not yet been demonstrated. Related previous works have included studies of the composition spectrum of perovskite $Sr_xLa_{1-x}Mn_yAl_{1-y}O_3$ (SLMA)[3] and of a few simple perovskites ($LaBO_3$, B=Mn, Co, Ni)[6] which found the composition dependence of the Fermi energy E_F relative to the O *2p* band center to be the dominant contribution to the composition dependence of E_V. This E_V descriptor, however, was observed to be applicable only for compounds without a band gap. Other studies of binary oxides and nitrides with a range of crystal structures reported a linear correlation between E_V and the band gap energy for compounds with finite band gaps and localized V_O-induced defect states.[7,8] Delocalized defect states were not accurately described by the same E_V descriptor, and although Tanaka *et al.*[7] suggested that E_V may be dependent on both the band gap energy and the structure and nature of bonds in the oxide, no corresponding descriptor was provided. A study of layered multicomponent oxides ($InAMO_4$, A=Al or Ga, M=Ca or Zn) and the corresponding binary oxide constituents demonstrated a qualitative E_V dependence on the cation ability to relax in response to anisotropic local environments created by the vacancy and the strength of the metal-oxygen bonds, as indicated by the constituent oxide enthalpies of formation.[9] Again, no related descriptor was provided. Finally, a study of $La_xSr_{1-x}BO_3$ perovskites (B=Cr, Mn, Fe, Co, Ni) reported a linear combination of the oxide enthalpy of formation and the minimum band gap

energy to be an accurate descriptor of E_V for nonmetallic oxides.[2] This E_V descriptor did not, however, extend as accurately to metallic oxides and again was demonstrated for a specific set of similar materials.

In this work, we use first principles quantum mechanical methods to investigate the fundamental phenomena associated with V_O formation and its material dependence across a broad range of compositions and crystal structures. We first examine intrinsic bulk material properties which describe E_V in perovskite oxides and find that, for small band gap perovskites, a combination of the oxide enthalpy of formation and the energy of the lowest unoccupied state relative to the O *2p* band center accurately correlate with E_V. For larger band gap oxides, a combination of the oxide enthalpy of formation and the minimum band gap energy correlate with E_V. We use both DFT+U and more accurate GW band gap energies to confirm the accuracy of these descriptors. Finally, we demonstrate $\Delta H_{f,oxide}$ and the band gap energy to be accurate descriptors of E_V for a broad range of oxides with GW band gaps greater than 1 eV including those with perovskite, antifluorite, corundum, rock salt, and rutile crystal structures.

Surprisingly, the physical mechanisms that contribute most significantly to E_V are quite simple and broadly applicable. Namely, E_V increases with increasing metal-oxygen bond strength and/or increasing V_O electron redistribution energy, as indicated by more negative $\Delta H_{f,oxide}$ and larger band gap energies (or, for small band gap materials, larger energy differences between the lowest unoccupied state and the O *2p* band center), respectively. These findings provide a valuable method for predicting E_V using purely intrinsic bulk properties and can be applied to efficiently search for new oxide materials with desired E_V properties.

4.3 Results

Herein, we first examine intrinsic bulk material properties which accurately describe E_V in perovskite oxides. We confirm the accuracy of these descriptors with more accurate GW band gap calculations and then demonstrate their broad applicability across variations in composition including different crystal structures.

We calculate charge neutral oxygen vacancy formation energies E_V at standard conditions using the standard supercell approach based on DFT+U[10] according to

$$E_V = E_{tot}^{defect} - E_{tot}^{host} + \mu_O^{FERE}$$

where E_o^{defect} and E_o^{host} are the total energies of the oxygen deficient (defect) and stoichiometric (host) supercells, respectively, and μ_O^{FERE} is the standard state oxygen chemical potential derived from the FERE[11] approach (see Computational Details). The formation of a charge neutral oxygen vacancy V_O involves the breaking of metal-oxygen bonds in order to remove a neutral oxygen atom. The resultant V_O-containing supercell is charge neutral, but the O *2p* electron density previously associated with the oxygen ion (two electrons) requires both spatial and energetic redistribution. For oxides without a band gap, these O *2p* electrons are transferred to unoccupied states at the Fermi energy E_F. For insulators, however, the O *2p* electrons from V_O formation populate the conduction band edge or V_O-induced defect states within the band gap. As we will show, both bond strength and the energy for redistribution of the V_O electrons contribute to E_V.

4.3.1 Small band gap E_V descriptor for perovskites

For small band gap (E_G^{GW}≤1 eV) perovskites, E_V accurately correlates with a linear combination of the oxide enthalpy of formation $\Delta H_{f,oxide}$ and the energy of the lowest unoccupied state E_{LUS} relative to the O *2p* band center as shown in Figure 4.1(a). This correlation, with a root mean squared error RMSE=0.27 eV, gives insight into the dominant physical mechanisms which contribute to E_V. First, increasing the metal-oxygen bond strength relative to the elemental phase metal-metal bond strengths, as indicated by more negative $\Delta H_{f,oxide}$, results in increasing E_V due to the increased energetic cost of breaking bonds in order to remove an oxygen atom. Second, increasing the energy of the V_O electron redistribution, as indicated by the energy difference between the lowest unoccupied state and the O *2p* band center, also results in increasing E_V. These contributions to E_V are consistent with previous works.[2,3]

The compositions of the perovskites included in Figure 4.1 are provided in Appendix C (Table C.1) along with their calculated properties. The relative contributions of $\Delta H_{f,oxide}$ and $(E_{LUS} - \text{O } 2p \text{ band center})^{DFT+U}$ were obtained by multiple linear regression for perovskites with GW band gap energies E_G^{GW}≤1 eV. Here we use the more accurate GW band gap energies only to group compounds; DFT+U band gap energies are used for the fits. The energy of the

lowest unoccupied state relative to the O *2p* band center can be separated into two components i) the minimum band gap energy and ii) E_F relative to the O *2p* band center. Fitting for the separate components resulted in a 1:1.04 ratio between the coefficients for the band gap energy and E_F relative to the O *2p* band center; therefore, we have used a 1:1 ratio and combined these two contributions into a single term without loss of accuracy.

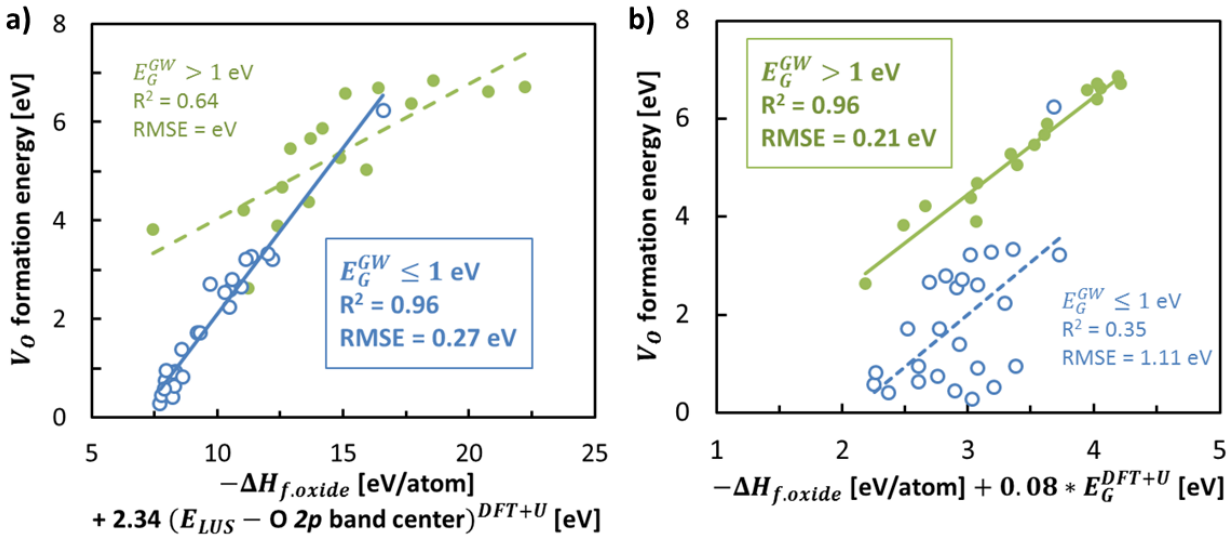

Figure 4.1 a) For small band gap (GW band gap energy E_G^{GW}≤1 eV) perovskites, oxygen vacancy formation energies E_V correlates with a combination of the oxide enthalpy of formation $\Delta H_{f,oxide}$ and the energy of the lowest unoccupied state E_{LUS} relative to the O 2p band center. b) For larger band gap (E_G^{GW}>1 eV) perovskites, oxygen vacancy formation energies E_V accurately correlates with a linear combination of the oxide enthalpy of formation $\Delta H_{f,oxide}$ and the band gap energy E_G^{DFT+U}. Closed symbols indicate perovskites with E_G^{GW}>1 eV; open symbols indicate E_G^{GW}≤1 eV.

The small band gap E_V descriptor provided in Figure 4.1(a) accurately applies for a broad range of small band gap perovskite compounds. Previous studies of perovskite $Sr_xLa_{1-x}Mn_yAl_{1-y}O_3$ (SLMA)[3] and of a few simple perovskites ($LaBO_3$, B=Mn, Co, Ni)[6] reported E_F relative to the O *2p* band center as the dominant contribution to the composition dependence of E_V. This single component descriptor, although accurate for SLMA and some $LaBO_3$ compositions without a band gap, cannot account for the effects of finite band gaps or wider variations in composition. Other studies have reported a linear correlation between E_V and the band gap energy for compounds with a band gap and localized V_O-induced defect states[7,8] but were also unable to accurately describe a broader range of materials. In contrast, the data set reported

here, which includes perovskites with and without band gaps, demonstrates the significance of the contributions of both the band gap energy and E_F relative to the O *2p* band center to the electron redistribution energy and, therefore, to the material dependence of E_V. In addition, this broader composition spectrum reveals the contribution of $\Delta H_{f,oxide}$ as an indicator of bond strength differences between materials. Ultimately, all three of these bulk material properties: $\Delta H_{f,oxide}$, the band gap energy, and E_F relative to the O *2p* band center, are significant contributors to the E_V descriptor for small band gap perovskites.

The E_V of larger band gap perovskites (E_G^{GW}>1 eV) are not well described by the same linear combination of $\Delta H_{f,oxide}$ and $(E_{LUS} - \text{O } 2p \text{ band center})^{DFT+U}$ as the E_V of small band gap perovskites (Figure 4.1(a)). As discussed in detail below, the energy of the lowest unoccupied state relative to the O *2p* band center becomes a less accurate descriptor of E_V for larger band gap perovskites, and alternatively, a combination of $\Delta H_{f,oxide}$ and the band gap energy provide an accurate E_V descriptor. The transition from one regime to the other results in E_V for perovskites with intermediate band gaps (e.g. those with ~0.5<E_G^{GW}<~2 eV) which accurately correlate with both the small or large band gap E_V descriptors.

4.3.2 Larger band gap E_V descriptor for perovskites

For larger band gap (E_G^{GW}>1 eV) perovskites, E_V accurately correlates with a linear combination of the oxide enthalpy of formation $\Delta H_{f,oxide}$ and the minimum band gap energy E_G^{DFT+U} with a RMSE=0.21 eV, as shown in Figure 4.1(b). Again, here we use the more accurate GW band gap energies only to group compounds; DFT+U band gap energies are used for the fits. As with small band gap perovskites, increasing the metal-oxygen bond strength, as indicated by more negative $\Delta H_{f,oxide}$, results in increasing E_V. Additionally, increasing the energy of the V_O electron redistribution again results in increasing E_V. However, for larger band gap perovskites, the energy of the lowest unoccupied state relative to the O *2p* band center becomes a less accurate descriptor of E_V. In fact, multiple linear regression analysis of E_V as a function of $\Delta H_{f,oxide}$, the band gap energy, and E_F relative to the O *2p* band center results in a positive coefficient for E_F relative to the O *2p* band center contribution indicating that a decrease in the electron redistribution energy contributes to an increase in E_V. Omitting the nonphysical contribution of E_F relative to the O *2p* band center yields a decrease in R^2 from

0.99 to 0.97 and an increase in the RMSE from 0.16 to 0.22 eV, both of which are tolerable. As a result, the E_V of larger band gap perovskites are best physically and accurately described by $\Delta H_{f,oxide}$ and the band gap energy.

Also shown in Figure 4.1(b), the larger band gap E_V descriptor is not accurate for small band gap perovskites because of the absence of the contribution of E_F relative to the O *2p* band center, which we have shown to be a dominant contributor to the electron redistribution energy for small band gap perovskites. In contrast, for larger band gap perovskites, $\Delta H_{f,oxide}$ is the dominant contributor to E_V and only a small fraction of E_G^{DFT+U} is required for an improved correlation. We propose that this relation arises due to variability in the electron redistribution energy for larger band gap materials. As previously discussed, for insulators, the electrons from V_O formation populate the conduction band edge or V_O-induced defect states within the band gap. As a result, a complex interplay exists between the energies of the O *2p* band center, the V_O-induced defect states, and the lowest unoccupied states. Interestingly, however, the larger band gap E_V descriptor suggests that these components largely compensate for one another such that the E_V of larger band gap perovskites are primarily described by $\Delta H_{f,oxide}$.

In addition to serving as an approximate indicator of the electron redistribution energy, the band gap energy can also relate to the metal-oxygen bond strength. From the tight bonding model for the formation of bands in solids, increased interatomic spacing and the resultant decreased strength of the overlap interaction between neighboring atoms results in decreased band width.[12–14] The gap between bands can be larger for small band widths such that larger band gap energies can indicate increased interatomic spacing due to decreased bond strength. However, for the larger band gap E_V descriptor provided in Figure 4.1(b), larger band gap energies correlate with larger E_V which is not consistent with decreased metal-oxygen bond strengths. Therefore, we conclude that the $\Delta H_{f,oxide}$ term in this E_V descriptor provides the dominant contribution to the metal-oxygen bond strength while the band gap energy weakly reflects the electron redistribution energy.

The larger band gap E_V descriptor provided in Figure 4.1(b) accurately applies for a broad range of larger band gap perovskite compounds. A similar study of $La_xSr_{1-x}BO_3$ perovskites (B=Cr, Mn, Fe, Co, Ni) also reported a linear combination of $\Delta H_{f,oxide}$ and the band

gap energy to be an accurate descriptor of E_V for nonmetallic oxides.[2] However, the broader variation in compositions included in this work extends that relation and provides more broadly applicable coefficients for the relative contributions of $\Delta H_{f,oxide}$ and E_G^{DFT+U}.

4.3.3 E_V descriptors from more accurate band gaps

Our previous analysis and discussion has utilized DFT+U band gap energies; however, it is well known that DFT commonly fails to accurately predict band gap energies. Alternatively, we now implement many-body GW calculations of electronic structure for a systematic improvement in band gap energies.[15–18] Employing a similar multiple linear regression analysis with more accurate GW minimum band gap energies E_G^{GW}, we again find that the E_V of larger band gap perovskites correlates with a combination of $\Delta H_{f,oxide}$ and the band gap energy, as shown in Figure 4.2. As with the DFT+U band gaps, $\Delta H_{f,oxide}$ is confirmed to be the dominant contributor to E_V and only a small fraction of E_G^{GW} is required.

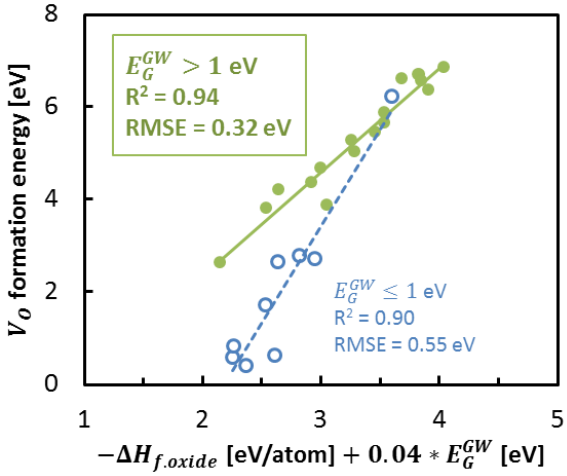

Figure 4.2 Calculated oxygen vacancy formation energies E_V accurately correlate with a linear combination of the oxide enthalpy of formation $\Delta H_{f,oxide}$ and the more accurate GW band gap energy E_G^{GW}. Closed symbols indicate perovskites with E_G^{GW}>1 eV; open symbols indicate E_G^{GW}≤1 eV.

The increased computational cost of GW calculations excludes $Sr_xLa_{1-x}Mn_yAl_{1-y}O_3$ (SLMA) compounds from the GW band gap analysis because of their large supercells and prohibitive cost. Interestingly, without the SLMA compounds, the subset of small band gap perovskites shown in Figure 4.2 is also reasonably well described, with a different slope and intercept, by the larger band gap E_V descriptor. This trend suggests that the E_V of these perovskites are also

less dependent on the contribution of E_F relative to the O *2p* band center. Further examination of Figure 4.1(b) also reveals a weak E_V correlation (R^2=0.85, RMSE=0.55 eV) with $\Delta H_{f,oxide}$ and E_G^{DFT+U} for small band gap perovskite compounds that do not have acceptor dopant (e.g. Sr-substitution onto La sites) concentrations equal to or in excess of their transition metal concentrations. In other words, a weak correlation is observed upon exclusion of SLMA compositions that have Sr mole fractions greater than or equal to that of Mn. Previous work[3] indicates that such SLMA compositions exhibit O *2p* electron hole character which we suggest may make the E_V of such compositions particularly sensitive to the contribution of E_F relative to the O *2p* band center. Consequently, small band gap perovskites without O *2p* electron hole character are moderately well described by the larger band gap E_V descriptor (albeit with a different slope and intercept). Nevertheless, because it provides a stronger correlation that applies to all small band gap perovskites considered here, the small band gap E_V descriptor from Figure 4.1(a) is preferred for small band gap perovskites. Without GW calculations for the SLMA compounds, we cannot accurately fit a broadly applicable small band gap E_V descriptor based on GW band gap energies.

4.3.4 E_V descriptor for other oxide crystal structures

We have demonstrated a combination of intrinsic bulk material properties, $\Delta H_{f,oxide}$ and the band gap energy, to be accurate descriptors of E_V for a broad range of perovskite compounds with E_G^{GW}>1 eV. As shown in Figure 4.3, this descriptor also applies more broadly to other oxides with E_G^{GW}>1 eV including those with antifluorite, corundum, rock salt, and rutile crystal structures. The coefficient for the band gap energy contribution has been optimized to maximize the average of the R^2 values and give strong correlations within each crystal structure group.

The universal applicability of this E_V descriptor for larger band gap oxides (E_G^{GW}>1 eV) arises from and confirms the dominant physical mechanisms which contribute to E_V. Namely, increasing E_V result from increasing the metal-oxygen bond strength and/or increasing the V_O electron redistribution energy, as indicated by more negative $\Delta H_{f,oxide}$ and larger band gap energies, respectively. These findings extend our understanding of the dominant contributions to V_O formation energetics in oxides and provide a valuable method for predicting E_V using

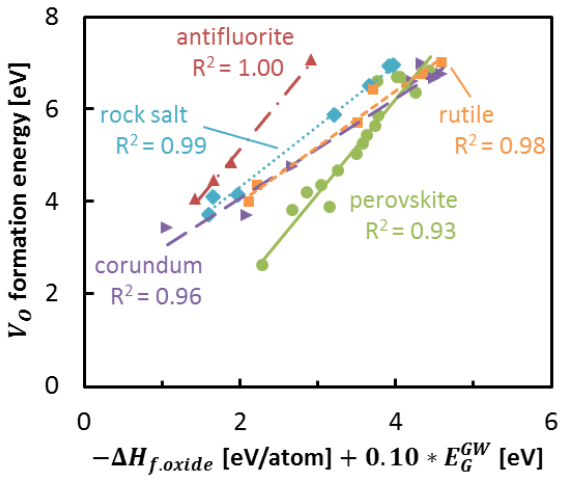

Figure 4.3 Calculated oxygen vacancy formation energies E_V for a range of oxide crystal structures accurately correlate with a linear combination of the oxide enthalpy of formation $\Delta H_{f,oxide}$ and the GW band gap energy E_G^{GW}. This correlation demonstrates the universal applicability of these intrinsic bulk material properties in describing the dominant physical mechanisms which contribute to E_V.

purely intrinsic bulk properties. Further validation of the predictive capabilities of both the small and larger band gap E_V descriptors presented here and their applicability to even broader material sets are ongoing (to be presented elsewhere).

4.4 Conclusions

We have presented an increased understanding of the relationship between oxygen vacancy formation energies E_V and the intrinsic bulk properties of oxides. Specifically, the E_V of larger band gap oxides (E_G^{GW}>1 eV) including those with perovskite, antifluorite, corundum, rock salt, and rutile crystal structures, accurately correlate with a combination of the oxide enthalpy of formation $\Delta H_{f,oxide}$ and the band gap energy. This relation arises from the contributions of the metal-oxygen bond strengths, as indicated by $\Delta H_{f,oxide}$, and the energetic redistribution of the oxygen vacancy electrons, as indicated by the band gap energy. Similarly, for small band gap perovskites (E_G^{GW}≤1 eV), calculated E_V correlate with a combination of $\Delta H_{f,oxide}$ and the energy of the lowest unoccupied state relative to the O *2p* band center, where the latter also corresponds to the energy for redistribution of the oxygen vacancy electrons.

These two simple, easily predicted descriptors provide a fundamental description of the dominant contributions to oxygen vacancy formation energies. Our results are consistent with

previous works, yet significantly broaden the range of oxide materials for which these descriptors accurately apply. We propose that the provided E_V descriptors be used to efficiently search for new oxide materials with desired E_V properties for a broad range of important energy applications which depend critically on the participation of oxygen vacancies including solar thermochemical fuel production cycles, solid oxide fuel cells, oxygen separation membranes, and catalytic membrane reactors.

4.5 Computational details

Spin polarized DFT+U[19] calculations were performed using a plane wave basis set, the PBE exchange-correlation functional,[20] and the projector augmented wave (PAW) method[21] as implemented in the Vienna Ab-initio Simulation Package (VASP).[22] A Monkhorst-Pack k-point sampling[23] was applied with a constant density corresponding to a 3x3x3 k-point mesh for a 40 atom unit cell resulting in total energies converged to within 3 meV/atom with respect to the number of k points. We chose an energy cutoff of 340 eV corresponding to a value ~20% greater than the highest cutoff energy suggested by the employed pseudopotentials (282 eV for oxygen). A constant U value of 3 eV was used for Sc, Ti, Cr, Mn, Fe, Co, Ni, Y, Zr, Rh, La, and Hf in accordance with the U values used for the fitted elemental-phase reference energies (FERE) method developed by Stevanović *et al.*[11] For all other elements, the Hubbard U parameter was set to zero. Spin degrees of freedom were treated explicitly. We performed a limited search for the DFT+U ground state spin configurations for Ti, Cr, Mn, Fe, Co, and Ni atoms. Magnetic moments were assigned at random and initialized with high spin values for both net zero antiferromagnetic (AFM) and ferromagnetic (FM) spin configurations. Experimentally determined magnetic configurations were used when available; otherwise, the lowest energy spin configurations were selected. All reported band gap energies correspond to minimum (fundamental) band gap energies.

For oxygen vacancy V_O calculations, supercells with 40-80 atoms were generated from experimental structures as recorded in the inorganic crystal structure database (ICSD).[24] Different supercell sizes result from differences in the unit cell size and symmetry. Both lattice parameters and atomic positions were optimized allowing for lattice distortions. Structures with an oxygen vacancy were created by removal of one neutral oxygen atom resulting in dilute

V_O concentrations of 2-6 %. Again, both lattice parameters and atomic positions were optimized. All nonequivalent O sites were sampled and averaged for binary and ternary compounds. For $La_{1-x}Sr_xBO_3$ (where B=Cr, Mn, Fe, Co, Ni) and $Sr_xLa_{1-x}Mn_yAl_{1-y}O_3$ (SLMA) compositions, nonequivalent O sites were sampled randomly as described in previous works.[2,3] From studies of $La_{1-x}Sr_xBO_3$, we find the oxygen vacancy formation energies E_V resulting from this scheme for 40 and 80 atom supercells (V_O concentrations = 4 and 2 %, respectively) to be converged to within 0.1 eV of the E_V for 160 atom supercells (V_O concentration = 1%) with the same geometry optimization procedure. However, as is the case for $Ba_{1-x}Sr_xCo_{1-y}Fe_yO_3$,[25,26] E_V is expected to increase with increasing oxygen nonstoichiometry such that the chosen nonstoichiometry range serves as a reference for dilute V_O concentrations. Additionally, from $LaCoO_3$ and $La_{0.6}Sr_{0.4}CoO_3$, the E_V differences between isolated V_O defects and V_O clusters (two neighboring V_O per cell) were calculated to be on the order of ≤0.2 eV/V_O indicating that the E_V of such systems are well represented by the E_V of isolated V_O defects.

The formation energy of a neutral oxygen vacancy (hereafter simply referred to as an oxygen vacancy) under standard conditions was calculated according to

$$E_V = E_{tot}^{defect} - E_{tot}^{host} + \mu_O^{FERE}$$

where E_o^{defect} and E_o^{host} are the total energies of the oxygen deficient (defect) and stoichiometric (host) supercells, respectively, and μ_O^{FERE} is the standard state oxygen chemical potential derived from the FERE[11] approach. Image charge and potential-alignment corrections[10] were not used due to the explicit charge neutrality of the supercells. Incomplete error cancelation occurs in DFT total energy differences of chemically dissimilar systems such as metals, semiconductors, insulators, and/or gaseous molecules. Alternatively, to correct for errors in the relative energies, the FERE energies, which have been fit to improve calculated standard state enthalpies of formation, were used. Therefore, our predicted E_V values, as provided in Table C.1, correspond closely to V_O formation energies under standard temperature and pressure conditions (298 K, 1 atm). The temperature and/or oxygen partial pressure dependences of E_V, which are largely independent of oxide composition, can be approximated by addition of the corresponding change in oxygen chemical potential using the ideal-gas equation of state under the assumption of neglecting vibrational degrees of freedom.[11] The

calculated values of E_V do not include solid state configurational entropies or thermal corrections due to heat capacity differences between the stoichiometric and oxygen deficient solid state phases, consistent with standard computational approaches for defects in solids.[10] Because these contributions are similar for stoichiometric and oxygen deficient supercells of the same composition, the solid state configurational entropies and thermal corrections at 298 K mostly cancel such that E_V accurately matches V_O formation energies at 298 K. This is consistent with computational studies of $SrTiO_3$, ZnO, and $La_{1-x}Sr_xCo_{1-y}Fe_yO_3$ which indicate that phonon contributions to the free energy of V_O formation are small at 298 K and tend to remain relatively small (<0.3 eV) for low oxygen nonstoichiometries (<12 % V_O) even at high temperatures (>1200 K).[27,28]

The enthalpies of formation of the oxides from their constituent elements $\Delta H_{f,oxide}$, as provided in Table C.1, were also calculated at 298 K using the total energies of the stoichiometric compositions and the FERE energies of the constituent elements where

$$\Delta H_{f,oxide} = E_{tot}^{host} - \sum_i c_i * \mu_i^{FERE}$$

Here, c_i corresponds to the mole fraction of each element present in the stoichiometric compound. The energies of the O *2p* band centers (also provided in Table C.1) were calculated from the DFT+U O PDOS as the center of mass of the O *2p* band including, when relevant, states above the Fermi energy but excluding O *2p* states hybridized with transition metal states.

Spin polarized GW band gap calculations were also performed within the PAW implementation of the VASP code. The crystal structures were relaxed with DFT+U, as detailed above, to obtain the initial DFT+U eigenenergies and wave functions prior to the quasiparticle energy (QPE) calculations in GW. Occupation-independent on-site potentials were utilized for the Ti, Cr, Mn, Fe, Co, and Ni transition metal *3d* states for improved agreement with experimental band gap energies according to the method developed by Lany.[18] A similar on-site potential of -5 eV was applied for the La *f* states from fitting to the experimental band gap of $LaAlO_3$. The same k-point sampling and energy cutoff used for DFT+U calculations were applied. The total number of bands was taken as 60 times the number of atoms in the unit cell. The resultant GW band gap energies are provided in Table C.1.

4.6 References

1. H. Peng, D. O. Scanlon, V. Stevanović, J. Vidal, G. W. Watson, and S. Lany, *Phys. Rev. B*, 2013, **88**, 115201.
2. A. M. Deml, V. Stevanović, C. L. Muhich, C. B. Musgrave, and R. O'Hayre, *Energy Environ. Sci.*, 2014, **7**, 1996–2004.
3. A. M. Deml, V. Stevanović, A. M. Holder, M. Sanders, C. B. Musgrave, and R. O'Hayre, *Nat. Commun.* (submitted).
4. R. Merkle, Y. A. Mastrikov, E. A. Kotomin, M. M. Kuklja, and J. Maier, *J. Electrochem. Soc.*, 2012, **159**, B219–B226.
5. Y. A. Mastrikov, R. Merkle, E. A. Kotomin, M. M. Kuklja, and J. Maier, *Phys. Chem. Chem. Phys.*, 2013, **15**, 911–918.
6. Y.-L. Lee, J. Kleis, J. Rossmeisl, Y. Shao-Horn, and D. Morgan, *Energy Environ. Sci.*, 2011, **4**, 3966–3970.
7. I. Tanaka, K. Tatsumi, M. Nakano, H. Adachi, and F. Oba, *J. Am. Ceram. Soc.*, 2002, **85**, 68–74.
8. T. Yamamoto and T. Mizoguchi, *Ceram. Int.*, 2013, **39**, S287–S292.
9. A. Murat and J. E. Medvedeva, *Phys. Rev. B*, 2012, **86**, 085123.
10. S. Lany and A. Zunger, *Phys. Rev. B*, 2008, **78**, 235104.
11. V. Stevanović, S. Lany, X. Zhang, and A. Zunger, *Phys. Rev. B*, 2012, **85**, 115104.
12. C. Kittel, *Introduction to Solid State Physics*, John Wiley & Sons, 8th Ed., 2005.
13. N. W. Ashcroft and N. D. Mermin, *Solid State Physics*, Brooks/Cole, Cengage Learning, 1976.
14. P. W. Atkins, *Quanta*, Oxford University Press, 2nd Ed., 1991.
15. M. Shishkin and G. Kresse, *Phys. Rev. B*, 2007, **75**, 235102.
16. M. Shishkin, M. Marsman, and G. Kresse, *Phys. Rev. Lett.*, 2007, **99**, 246403.
17. M. van Schilfgaarde, T. Kotani, and S. Faleev, *Phys. Rev. Lett.*, 2006, **96**, 226402.
18. S. Lany, *Phys. Rev. B*, 2013, **87**, 085112.
19. S. L. Dudarev, G. A. Botton, S. Y. Savrasov, C. J. Humphreys, and A. P. Sutton, *Phys. Rev. B*, 1998, **57**, 1505–1509.
20. J. P. Perdew, K. Burke, and M. Ernzerhof, *Phys. Rev. Lett.*, 1996, **77**, 3865–3868.
21. P. Blöchl, *Phys. Rev. B*, 1994, **50**, 17953–17979.
22. G. Kresse and J. Furthmüller, *Comput. Mater. Sci.*, 1996, **6**, 15–50.
23. H. Monkhorst and J. Pack, *Phys. Rev. B*, 1976, **13**, 5188–5192.

24. A. Belsky, M. Hellenbrandt, V. L. Karen, and P. Luksch, *Acta Crystallogr. Sect. B Struct. Sci.*, 2002, **B58**, 364–369.

25. E. A. Kotomin, Y. A. Mastrikov, M. M. Kuklja, R. Merkle, A. Roytburd, and J. Maier, *Solid State Ionics*, 2011, **188**, 1–5.

26. M. M. Kuklja, Y. A. Mastrikov, B. Jansang, and E. A. Kotomin, *J. Phys. Chem. C*, 2012, **116**, 18605–18611.

27. D. Gryaznov, M. W. Finnis, R. A. Evarestov, and J. Maier, *Solid State Ionics*, 2014, **254**, 11–16.

28. D. Gryaznov, E. Blokhin, A. Sorokine, E. A. Kotomin, R. A. Evarestov, A. Bussmann-holder, and J. Maier, *J. Phys. Chem. C*, 2013, **117**, 13776–13784.

CHAPTER 5

GENERAL CONCLUSIONS

We have presented a fundamental and unifying set of descriptors for oxygen vacancy formation energies E_V that applies across broad variations in oxide composition including different crystal structures. These findings provide a valuable method for efficiently predicting oxygen vacancy formation energies from intrinsic bulk material properties. For the complex perovskite $Sr_xLa_{1-x}Mn_yAl_{1-y}O_3$ (SLMA), predicted E_V for compositions without a band gap are shown to arise from differences in the Fermi energy relative to the O *2p* band center. For $La_{1-x}Sr_xBO_3$ perovskites (B=Cr, Mn, Fe, Co, and Ni) including those with finite band gap energies, a combination of two fundamental and intrinsic materials properties, the oxide enthalpy of formation $\Delta H_{f,oxide}$ and the minimum band gap energy, accurately correlate with E_V. These two perovskite systems, in combination with a broad range of other perovskite compositions, demonstrate the E_V of small band gap perovskites to be well described by a combination of $\Delta H_{f,oxide}$ and the energy of the lowest unoccupied state relative to the O *2p* band center while the E_V of larger band gap perovskites are accurately described by a combination of the $\Delta H_{f,oxide}$ and the minimum band gap energy. Finally, we demonstrate $\Delta H_{f,oxide}$ and the band gap energy to be accurate descriptors of E_V for a broad range of oxides with GW band gap energies greater than 1 eV including those with perovskite, antifluorite, corundum, rock salt, and rutile crystal structures.

This thesis work also extends our understanding of the dominant physical mechanisms contributing to oxygen vacancy formation energies thereby better enabling the design of new redox active materials. We show that oxygen vacancy formation energies increase with increasing metal-oxygen bond strength and/or increasing oxygen vacancy electron redistribution energy. Here, the bond strength contribution is closely related to the oxide enthalpy of formation and the electron redistribution energy contribution is described by either the band gap energy or, for small band gap materials, by the energy difference between the

lowest unoccupied state and the O *2p* band center. We suggest the application of this work for the informed design and study of novel oxide systems for a range of technological applications.

5.1 Recommendations for future research

Continued research in the area of oxygen vacancy formation energetics is of strong interest. Initial extensions of the work presented here should first aim to assess the predictive capability of the proposed E_V descriptors. To this aim, we recommend significant expansion of the current E_V data set, preferably via high-throughput automation, to include both a larger number of entries and a broader range of compositions. The proposed E_V descriptors can be used to predict the E_V of compounds to which they were not fit and thereby assessed for accuracy. Reparameterization of the proposed E_V descriptors may be considered if increased accuracy is desired. Additionally, an expanded data set provides the opportunity for data mining in order to examine, for example, crystal structure descriptors which could enable a set of E_V descriptors with a single fit that applies for all crystal structures.

With a strong and well validated set of E_V descriptors, we suggest the prediction of E_V for a large set of existing and/or new compounds using high-throughput bulk material property calculations. Several computational material databases (Open Quantum Materials Database,[1] oqmd.org; Materials Project,[2] materialsproject.org; NREL Materials Database[3]) presently include tens of thousands of material entries with the necessary data available to calculate FERE oxide enthalpies of formation, Fermi energies relative to the O *2p* band center, and band gap energies. These resources could be utilized to predict E_V and screen a tremendous number of compounds for those with desired E_V properties for specific applications such as solar thermochemical fuel production cycles.

Finally, we suggest application of this improved understanding of the dominant physical mechanisms contributing to E_V for the informed design of complex oxide systems. For example, the electronic structure origins of the tunable E_V in the $Sr_xLa_{1-x}Mn_yAl_{1-y}O_3$ system, discussed in Chapter 2, serve as an excellent model of the mechanisms by which to design and optimize oxide compositions. These design principles can be applied to other complex oxides of interest particularly when the multivariate compositional freedom impedes exhaustive experimental optimization.

5.2 References

1. J. E. Saal, S. Kirklin, M. Aykol, B. Meredig, and C. Wolverton, *JOM*, 2013, **65**, 1501–1509.
2. A. Jain, G. Hautier, C. J. Moore, S. Ping Ong, C. C. Fischer, T. Mueller, K. A. Persson, and G. Ceder, *Comput. Mater. Sci*., 2011, **50**, 2295–2310.
3. To be presented elsewhere.

APPENDIX A

CHAPTER 2 SUPPLEMENTARY INFORMATION

Herein, we provide supplementary information for "Chapter 2: Tunable oxygen vacancy formation energetics in the complex perovskite oxide $Sr_xLa_{1-x}Mn_yAl_{1-y}O_3$."

A.1 Experimental oxygen vacancy formation energies

The negative of the temperature-independent reaction enthalpies for oxidation by $O_{2(g)}$ correspond to oxygen vacancy formation energies E_V. For example, the $LaMnO_3$ oxidation reaction is given in Kroger-Vink notation by $\frac{1}{2}O_{2(g)} + V_O^{\cdot\cdot} + 2Mn'_{Mn} \rightarrow O_O^x + 2Mn_{Mn}^x$. Measured reaction enthalpies for oxidation by $O_{2(g)}$ are reported in the main article for $LaMnO_3$ (LM)[1] and $La_{0.6}Sr_{0.4}MnO_3$ (LSM64)[2] compositions with δ=0.01 and δ=0.1, respectively. For a consistent comparison, the effects of charge disproportionation (e.g. $2Mn^{3+} = Mn^{4+} + Mn^{2+}$) are excluded from the measured values because these effects are not accounted for in our calculations at 0 K.

A.2 Calculated total and partial densities of states

Calculated total (TDOS) and partial densities of states (PDOS) for the SLMA composition spectrum (Figure A.1) illustrate connections between the trends in oxygen vacancy formation energies E_V and the corresponding electronic structure changes as summarized schematically in Figure 2.3(b). Here, specific $Sr_xLa_{1-x}Mn_yAl_{1-y}O_3$ compositions are denoted as SLMA$\alpha\beta\gamma\varepsilon$, e.g. SLMA2846 denotes a composition of $Sr_{0.2}La_{0.8}Mn_{0.4}Al_{0.6}O_3$. Different cation configurations give small variations in the TDOS and PDOS, but characteristic features remain consistent. Sr and Al PDOS are negligible over these energy ranges and have been omitted.

A.3 Bader electronic charge distributions on Mn and O ions

Electronic charge distributions on Mn and O ions, as shown in Figure A.2, are also valuable for examining the electronic structure differences across the SLMA composition spectrum. More positive average Bader charge per Mn ion Q_{Mn} indicates greater Mn hole density per ion (i.e. less reduction of Mn). Likewise, for a constant mole fraction of Mn, less negative average Bader charge per O ion Q_O indicates greater O hole density per ion (i.e. less reduction of

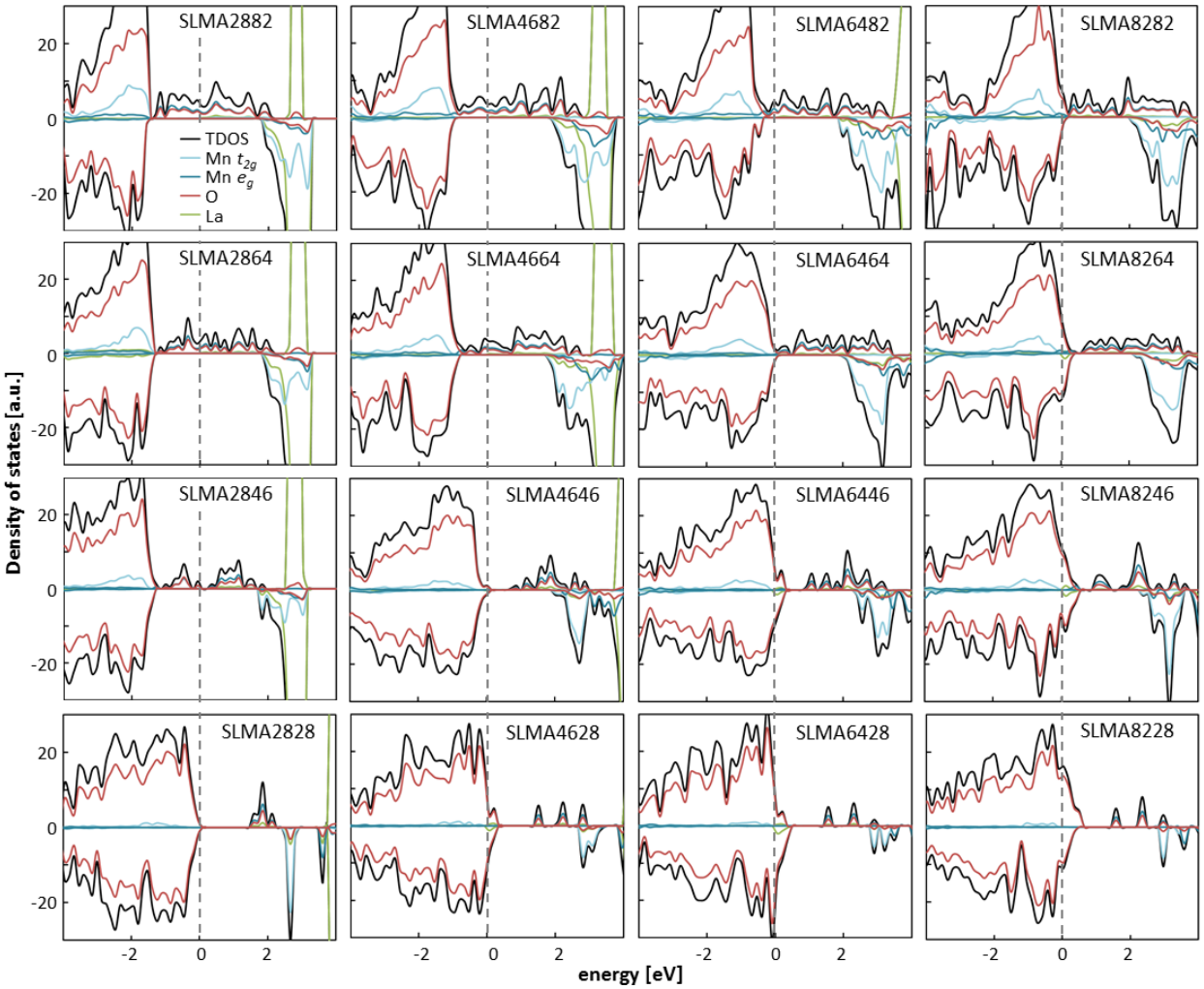

Figure A.1 Calculated densities of states. Calculated total (TDOS) and partial densities of states (PDOS) for the SLMA composition spectrum illustrate connections between the trends in oxygen vacancy formation energies E_V and the corresponding electronic structure changes. Panels are organized with increasing Sr mole fraction from left to right and increasing Mn mole fraction from bottom to top. The TDOS and PDOS color legend is provided in the upper left panel. The energy of the highest occupied state is aligned to zero. Spin-up and spin-down DOS are shown as positive and negative values, respectively.

O). With only two exceptions, all Q_{Mn} exhibit a standard deviation of ≤0.03 *e*/ion indicating that the electron density on Mn is well dispersed. The two exceptions, SLMA2846 and SLMA2864, exhibit some localization of electron density onto specific Mn sites leading to standard deviations in Q_{Mn} of 0.06 and 0.05 *e*/ion, respectively. The standard deviations for Q_O range from 0.08-0.16 *e*/ion, which indicates a greater variation in the O electron density distributions primarily as a result of variations in the local cation environment.

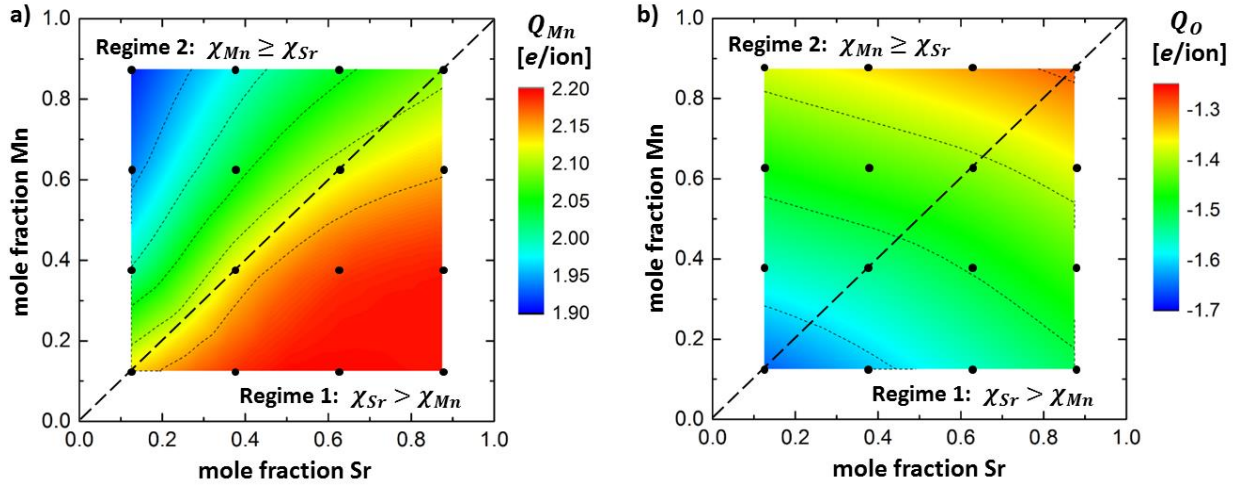

Figure A.2 Bader electronic charge distributions on Mn and O ions. As descriptors of the electronic structure differences across the SLMA composition spectrum, calculated average Bader charges a) per Mn ion Q_{Mn} and b) per O ion Q_O impact oxygen vacancy formation energetics. More positive Q_{Mn} indicate greater Mn hole density per ion while, for a constant Mn mole fraction, less negative Q_O indicate greater O hole density per ion. Differences in the average B-O bond covalency accompanying different Mn mole fractions require that additional information be used in such cases to determine changes in the degree of O reduction. Calculated compositions are marked by black points.

A.3.1 Differences between Regimes 1 and 2

Within Regime 1, Q_{Mn} is most positive and predicted to be approximately constant indicating that Mn ions reach an effective saturation limit beyond which less electron density (i.e. greater hole density) per Mn ion is unfavorable. This arises due to the high mole fraction of Sr χ_{Sr} and corresponding high hole concentration from Sr-substitution that cannot be fully accommodated by the smaller mole fraction of Mn χ_{Mn}. This behavior is consistent with the fully unoccupied Mn-O band in Regime 1 as shown in Figure 2.3(b). Within Regime 2, Q_{Mn} is below its saturation limit indicating that the high χ_{Mn} can accommodate the holes from the smaller χ_{Sr}, which is consistent with the partially occupied Mn-O band of Regime 2 shown in

Figure 2.3(b). Variations in Q_O are more complex and will be examined in detail throughout the following discussion.

Although applicable for a constant χ_{Mn}, the simple relation that less negative Q_O indicates less electron density (i.e. greater hole density) per O ion does not necessarily hold for compositions with different χ_{Mn} due to the resultant changes in the B-O bond character. In contrast to the highly ionic Al-O bonds, Mn-O bonds are partially covalent which causes an increase in shared electron density between Mn and O in comparison to Al and O. The partial covalent nature of the Mn-O bonds[3–5] is evidenced by the significant difference between Mn and O formal oxidation states and the calculated Q_{Mn} and Q_O, respectively. As a result, different χ_{Mn} exhibit different average B-O bond covalencies. For example, compositions with greater χ_{Mn} exhibit greater average B-O bond covalency resulting in a less negative Q_O due to the increase in shared electron density between Mn and O. Simultaneously, the increase in χ_{Mn} allows for greater fraction of hole density of Mn character, yielding an actual decrease in hole density per O ion and more negative Q_O. Therefore, when comparing compositions with different χ_{Mn}, information regarding the Mn electron density is needed in order to determine the resultant changes in O hole density.

A.3.2 Increasing χ_{Sr} with constant χ_{Mn}

The V_O formation mechanisms observed for increasing χ_{Sr} with constant χ_{Mn}, where decreases in the energy difference between the Fermi energy E_F and the O *2p* band center decrease E_V, are also evidenced by changes in Q_{Mn} and Q_O. As previously mentioned, within Regime 1 Q_{Mn} is effectively saturated and greater hole density per Mn ion is unfavorable. As a result, to compensate for a higher Sr concentration, the O hole density increases with increasing χ_{Sr} as indicated by the less negative Q_O in Figure A.2(b). This increase in O hole density is equivalent to the downward shift of E_F within the O *2p* band and the corresponding decrease in E_F relative to the O *2p* band center (Figure 2.3(b)) which decreases E_V. Within Regime 2, Q_{Mn} is below its saturation limit such that both Mn and O hole densities per ion increase with increasing χ_{Sr}, as indicated by the more positive Q_{Mn} and less negative Q_O. This behavior is equivalent to the downward shift of E_F within the Mn-O band and the corresponding decrease in E_F relative to the O *2p* band center (Figure 2.3(b)) which decreases

E_V. A slight bend in the Q_O contour lines where $\chi_{Mn} = \chi_{Sr}$ illustrates the increasing fraction of holes that are provided by O as Q_{Mn} reaches saturation and Mn no longer provides additional hole density.

A.3.3 Increasing χ_{Mn} with constant χ_{Sr}

Again, the V_O formation mechanisms for increasing χ_{Mn} with constant χ_{Sr}, where decreases in the energy difference between E_F and the O *2p* band center decrease E_V and vice versa, are also evidenced by changes in Q_{Mn} and Q_O. The constant hole concentration due to Sr-substitution results in a constant cumulative hole density on Mn and O. Within Regime 1, Q_{Mn} is saturated and approximately constant. However, with the increase in χ_{Mn}, the total Mn hole density increases, and the remaining hole density required from O decreases. The apparent inconsistency between this decrease in the hole density per O and the less negative Q_O, as shown in Figure A.2(b), arises from an increase in the average B-O bond covalency. Because E_F lies within the O *2p* band in Regime 1, the decreasing O hole density, or equivalently the upward shift of E_F and the corresponding increase in E_F relative to the O *2p* band center, results in increasing E_V.

Within Regime 2, Q_{Mn} is below its saturation limit and increasing χ_{Mn} results in less hole density per Mn ion (less positive Q_{Mn}) because the hole density from Sr-substitution is distributed across additional Mn. As in Regime 1, the increase in χ_{Mn} increases the total Mn hole density despite the decrease per Mn ion. The constant χ_{Sr} and corresponding constant cumulative hole density on Mn and O results in a decrease in the O hole density (again, despite the less negative Q_O). Because E_F lies within the Mn-O band in Regime 2, this constant cumulative hole density on Mn and O, or equivalently the constant energy of E_F relative to the O *2p* band center, results in a constant E_V.

A.4 References

1. J. H. Kuo, H. U. Anderson, and D. M. Sparlin, *J. Solid State Chem.*, 1989, **83**, 52–60.
2. J. Mizusaki, H. Tagawa, K. Naraya, and T. Sasamoto, *Solid State Ionics*, 1991, **49**, 111–118.
3. M. M. Kuklja, E. A. Kotomin, R. Merkle, Y. A. Mastrikov, and J. Maier, *Phys. Chem. Chem. Phys.*, 2013, **15**, 5443–5471.
4. J. He and C. Franchini, *Phys. Rev. B*, 2012, **86**, 235117.

5. J. Suntivich, H. a Gasteiger, N. Yabuuchi, H. Nakanishi, J. B. Goodenough, and Y. Shao-Horn, *Nat. Chem.*, 2011, **3**, 546–550.

APPENDIX B

CHAPTER 3 SUPPLEMENTARY INFORMATION

Herein, we provide supplementary information for "Chapter 3: Oxide enthalpy of formation and band gap energy as accurate descriptors of oxygen vacancy formation energetics."

B.1 Experimental oxygen vacancy formation energies

The temperature-independent oxidation reaction enthalpies correspond to the negative of the oxygen vacancy formation energies $-E_V$; in other words, the LB oxidation reactions are given by $\frac{1}{2}O_{2(g)} + V_O^{\cdot\cdot} + 2B_B^x \rightarrow O_O^x + 2B_B'$ and are reported in the main article for LB and LSB64 compositions with δ=0.01 and δ=0.1, respectively. For a consistent comparison, the effects of charge disproportionation (e.g. $2B^{3+} = B^{4+} + B^{2+}$) are excluded from the experimental reaction enthalpies because these effects are not accounted for in our calculations at 0 K.

B.2 Extrapolated and interpolated experimental values

The LSCr64 experimental E_V and $\Delta H_{f,oxide}$ that we report have been extrapolated from measured values for $La_{1-x}Sr_xCrO_3$ with x=0.1, 0.2, and 0.3.[1,2] The LSM64 experimental $\Delta H_{f,oxide}$ has been interpolated from measured values for $La_{1-x}Sr_xMnO_3$ with x=0.1, 0.3, and 0.5.

B.3 Additional results

Figure B.1 shows effective Bader charges on TM B and O ions in stoichiometric LB and LSB64 compositions. Significant differences between the effective charges on TM B and O ions and their formal oxidation states indicate the covalent nature of the B-O bonding. In addition, the nonlinear trend in the degree of covalency of the TM B-O bonds, which is indicated by the magnitude of the charge difference from the formal oxidation states, suggests that B-O bond covalency alone cannot account for the linear trends in the oxide enthalpies of formation $\Delta H_{f,oxide}$ as a function of the atomic number of B.

Figure B.2 shows the total densities of states (TDOS) for the stoichiometric and oxygen deficient LB and LSB compositions. Redistribution of the excess electrons due to oxygen vacancy V_O formation fills previously unoccupied states; consequently, a higher energy state

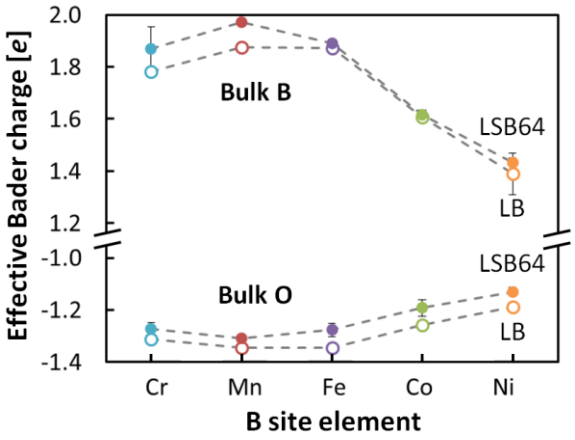

Figure B.1 Average effective Bader charges on TM B and O ions in stoichiometric LB and LSB64 compositions. La and Sr effective Bader charges are independent of composition with average values of 2.16 ± 0.01 and 1.59 ± 0.01 *e*, respectively.

becomes the highest occupied state and the corresponding energy of the highest occupied state E_{HOS} increases. The magnitude of the increase in E_{HOS} roughly trends with the magnitude of the energy difference between the lowest unoccupied state and the highest occupied state ΔE. As a result, the insulating LB compositions which exhibit large ΔE also exhibit large increases in E_{HOS} upon V_O formation which in turn contributes to high E_V. In contrast, the LSB64 compositions exhibit negligible ΔE due to the low energy unoccupied states created as a result of the Sr-substitution. These negligible ΔE significantly decrease E_V due to the corresponding small E_{HOS} increases.

As with cation configurations, different V_O configurations gave small variations in the oxygen deficient LSB64 DOS, but characteristic features remained consistent. The energy scale has been aligned so as to match the O *2s* core states. These results are consistent with previous calculations of $Ba_{0.5}Sr_{0.5}Co_{1-y}Fe_yO_3$[3] where the PDOS directly above E_{HOS} is higher for Co than for Fe resulting in lowered E_V with increasing fraction of Co.

Figure B.3 illustrates the correlation between E_V and the individual parameters $\Delta H_{f,oxide}$ and ΔE. The improved correlation of the combined $\Delta H_{f,oxide}$ and ΔE descriptor with E_V as compared to either of the individual parameters alone is reflected by increasing R^2 values of 0.67, 0.72, and 0.94 for linear regression fits for only $\Delta H_{f,oxide}$, only ΔE, and for the combined parameter, respectively.

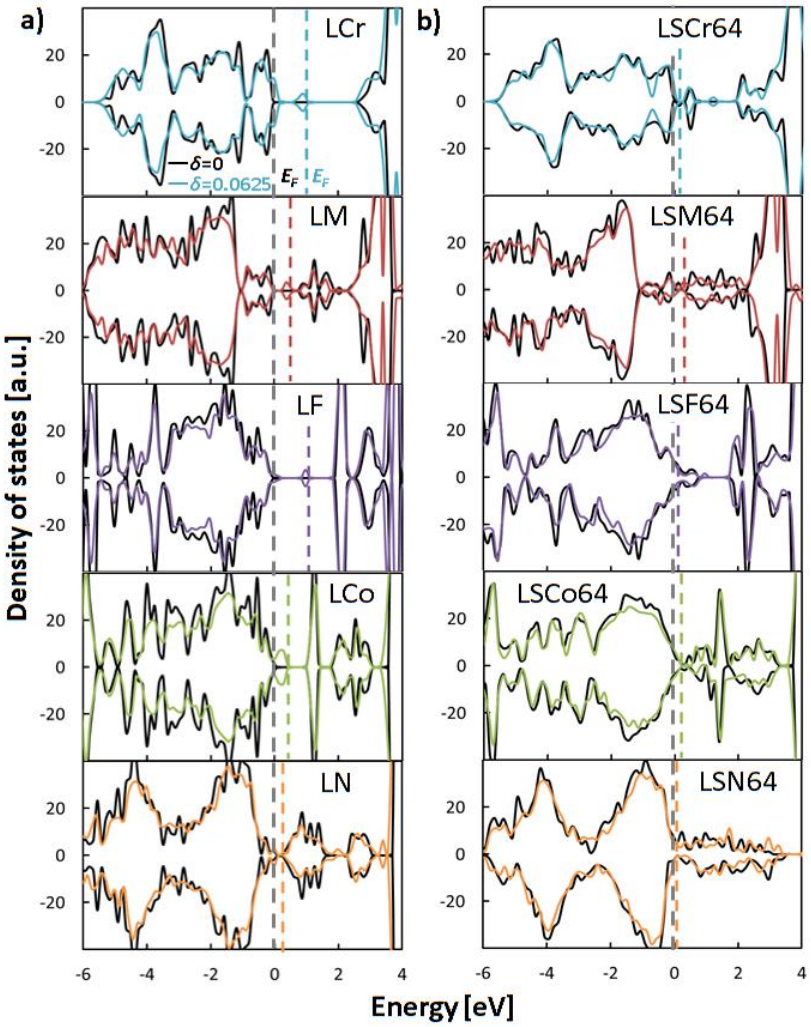

Figure B.2 Total densities of states for 80 atom stoichiometric (black, $\delta = 0$) and oxygen deficient (colored, $\delta = 0.0625$) a) LB and b) LSB64 compositions. The energy scale is adjusted to align the O *2s* states, and the corresponding energies of the highest occupied states are indicated by dashed lines. Spin-up and spin-down DOS are shown as positive and negative values, respectively.

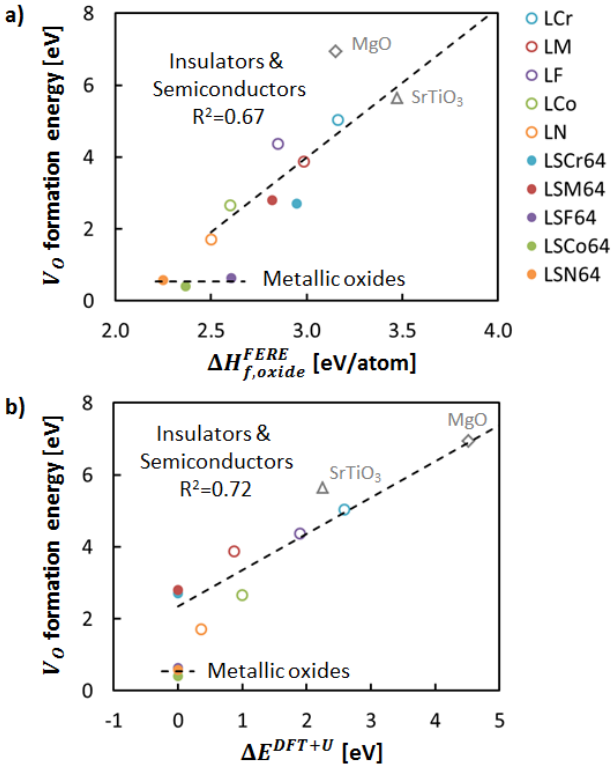

Figure B.3 Oxygen vacancy formation energies for LB and LSB64 compositions as a function of a) calculated oxide enthalpies of formation $\Delta H_{f,oxide}$ and b) calculated band gap energies calculated as the difference between the energies of the lowest unoccupied state and the highest occupied state ΔE. Only nonmetallic LB and LSB64 compositions were used in the fits, although the lines are extended for comparison with MgO and $SrTiO_3$. The corresponding R^2 values are provided for comparison with the R^2=0.94 for E_V as a function of the combined $\Delta H_{f,oxide}$ and ΔE parameter.

B.4 References

1. J. Mizusaki, S. Yamauchi, K. Fueki, and A. Ishikawa, *Solid State Ionics*, 1984, **12**, 119–124.
2. J. Cheng and A. Navrotsky, *J. Solid State Chem.*, 2005, **178**, 234–244.
3. E. A. Kotomin, Y. A. Mastrikov, M. M. Kuklja, R. Merkle, A. Roytburd, and J. Maier, *Solid State Ionics*, 2011, **188**, 1–5.

APPENDIX C

CHAPTER 4 SUPPLEMENTARY INFORMATION

Here, we provide tabulated data for "Chapter 4: Unifying descriptors of oxygen vacancy formation energies across a broad range of oxide compositions and structures."

Table C.1 Oxide compounds and their calculated properties: oxygen vacancy formation energy E_V, oxide enthalpy of formation $\Delta H_{f,oxide}$, Fermi energy E_F relative to the O *2p* band center, DFT+U minimum band gap energy E_G^{DFT+U}, and GW minimum band gap energy E_G^{GW}. The energy of the lowest unoccupied state relative to the O *2p* band center can be calculated as the band gap energy plus E_F relative to the O *2p* band center. Materials are sorted by crystal structure, then GW band gap energy. Specific $Sr_xLa_{1-x}Mn_yAl_{1-y}O_3$ compositions are denoted as SLMA$\alpha\beta\gamma\varepsilon$, e.g. SLMA2864 denotes a composition of $Sr_{0.2}La_{0.8}Mn_{0.6}Al_{0.4}O_3$. GW calculations were not performed for SLMA compositions; all SLMA compounds were grouped with the perovskites with E_G^{GW}≤1 eV and are sorted by composition.

Compound	**Crystal structure**	E_V **(eV)**	$\Delta H_{f,oxide}$ **(eV/atom)**	E_F **- O *2p* band center (eV)**	E_G^{DFT+U} **(eV)**	E_G^{GW} **(eV)**
SLMA2828	perovskite	3.2	-3.61	2.34	1.3	n/a
SLMA2846	perovskite	3.3	-3.36	3.67	0.0	n/a
SLMA2864	perovskite	3.3	-3.19	3.47	0.0	n/a
SLMA2882	perovskite	3.2	-3.02	3.45	0.0	n/a
SLMA4628	perovskite	0.9	-3.38	2.11	0.0	n/a
SLMA4646	perovskite	2.2	-3.24	2.49	0.6	n/a
SLMA4664	perovskite	2.6	-3.07	3.17	0.0	n/a
SLMA4682	perovskite	2.5	-2.91	3.14	0.0	n/a
SLMA6428	perovskite	0.5	-3.21	1.98	0.0	n/a
SLMA6446	perovskite	0.9	-3.07	2.19	0.0	n/a
SLMA6464	perovskite	1.4	-2.93	2.40	0.0	n/a
SLMA6482	perovskite	1.7	-2.77	2.73	0.0	n/a
SLMA8228	perovskite	0.3	-3.03	1.99	0.0	n/a
SLMA8246	perovskite	0.4	-2.90	2.07	0.0	n/a
SLMA8264	perovskite	0.7	-2.75	2.20	0.0	n/a
SLMA8282	perovskite	1.0	-2.61	2.27	0.0	n/a
$La_{0.6}Sr_{0.4}CrO_3$	perovskite	2.7	-2.95	2.88	0.0	0.0
$La_{0.6}Sr_{0.4}MnO_3$	perovskite	2.8	-2.82	3.30	0.0	0.0
$La_{0.6}Sr_{0.4}FeO_3$	perovskite	0.6	-2.61	2.42	0.0	0.0
$La_{0.6}Sr_{0.4}CoO_3$	perovskite	0.4	-2.37	2.48	0.0	0.0
$La_{0.6}Sr_{0.4}NiO_3$	perovskite	0.6	-2.25	2.39	0.0	0.0

Table C.1 Continued.

Compound	Crystal structure	E_V (eV)	$\Delta H_{f,oxide}$ (eV/atom)	E_F - O *2p* band center (eV)	E_G^{DFT+U} (eV)	E_G^{GW} (eV)
$SrFeO_3$	perovskite	0.8	-2.26	2.69	0.0	0.0
$LaNiO_3$	perovskite	1.7	-2.50	2.71	0.2	0.9
$LaCoO_3$	perovskite	2.7	-2.60	2.48	1.1	1.0
$LaTiO_3$	perovskite	6.2	-3.56	4.12	1.4	1.0
$ScAlO_3$	perovskite	6.6	-3.63	2.34	5.0	1.3
$LaMnO_3$	perovskite	3.9	-2.98	3.04	1.0	1.8
$LaFeO_3$	perovskite	4.4	-2.85	2.57	2.0	2.1
$HgTiO_3$	perovskite	2.6	-2.07	2.53	1.4	2.3
$BaSnO_3$	perovskite	3.8	-2.46	1.73	0.4	2.3
$BaTiO_3$	perovskite	5.4	-3.35	1.97	2.1	2.8
$YAlO_3$	perovskite	6.7	-3.72	2.12	5.8	3.1
$SrTiO_3$	perovskite	5.7	-3.42	2.14	2.2	3.2
$LaCrO_3$	perovskite	5.0	-3.16	2.76	2.7	3.4
$SrSnO_3$	perovskite	4.2	-2.51	1.85	1.8	3.7
$SrZrO_3$	perovskite	6.7	-3.68	1.36	4.1	3.9
$CaTiO_3$	perovskite	5.9	-3.40	1.89	2.7	3.9
$LaInO_3$	perovskite	4.7	-2.85	1.49	2.7	4.2
$BaZrO_3$	perovskite	6.6	-3.66	1.46	3.4	5.0
$LaGaO_3$	perovskite	5.3	-3.06	1.78	3.3	5.3
$LaAlO_3$	perovskite	6.4	-3.70	2.13	3.8	5.6
$SrHfO_3$	perovskite	6.8	-3.80	1.68	4.6	6.4
Rb_2O	antifluorite	4.1	-1.18	0.31	1.3	2.5
K_2O	antifluorite	4.5	-1.30	0.31	1.7	3.7
Na_2O	antifluorite	4.9	-1.46	0.50	1.9	4.3
Li_2O	antifluorite	7.1	-2.10	1.50	5.2	8.2
Rh_2O_3	corundum	3.4	-0.89	3.90	1.5	1.8
In_2O_3	corundum	3.7	-1.87	1.78	1.0	2.4
Ga_2O_3	corundum	4.8	-2.22	2.32	2.5	4.6
La_2O_3	corundum	6.6	-3.74	1.06	3.7	4.9
Y_2O_3	corundum	6.7	-3.90	1.06	4.2	6.1
Sc_2O_3	corundum	6.8	-3.85	1.61	4.6	7.5
Al_2O_3	corundum	7.0	-3.44	2.52	5.9	9.1

Table C.1 Continued.

CoO	rock salt	4.1	-1.34	3.36	2.1	3.2
NiO	rock salt	3.7	-1.26	3.19	2.2	3.5
BaO	rock salt	5.9	-2.86	0.79	2.1	3.5
FeO	rock salt	4.2	-1.54	3.91	1.3	4.4
SrO	rock salt	6.5	-3.11	0.91	3.3	5.6
CaO	rock salt	7.0	-3.27	1.15	3.6	7.0
MgO	rock salt	6.9	-3.13	1.87	4.5	7.9
SnO_2	rutile	4.0	-1.87	2.79	0.7	2.6
TiO_2	rutile	5.7	-3.24	2.82	2.1	2.9
GeO_2	rutile	4.4	-1.88	3.80	1.1	3.5
ZrO_2	rutile	6.8	-3.80	2.28	3.8	5.4
HfO_2	rutile	7.0	-3.98	2.45	4.2	6.2
SiO_2	rutile	6.4	-2.89	4.59	5.0	8.3